Atmospheric Cold Pools and Their Influence on Sea Surface Temperature in the Bay of Bengal

M. S. Girishkumar[1] , **Jofia Joseph[1,2], M. J. McPhaden[3]** , **and E. Pattabhi Ram Rao[1]**

[1]Indian National Centre for Ocean Information Services, Ministry of Earth Sciences, Hyderabad, India, [2]School of Ocean Science and Technology, Kerala University of Fisheries and Ocean Studies, Kochi, India, [3]Pacific Marine Environmental Laboratory, National Oceanic and Atmospheric Administration, Seattle, WA, USA

Abstract Recent observations show that atmospheric cold pool (ACP) events are plentiful in the Bay of Bengal (BoB) during summer (May–September) and fall (October–November) and that these events can significantly modify local air-sea interaction processes on sub-daily time scales. In this study, we examine whether the magnitude of sea surface temperature (SST) drop associated with ACP events shows any diurnal variability during summer and fall. For this purpose, we use moored buoy data with a 10-min temporal resolution at 8°, 12°, and 15°N along 90°E and a one-dimensional mixed layer (ML) model. The analysis shows a reduction in SST (ΔSST) due to ACPs in the BoB during summer and fall, with a maximum magnitude of ΔSST during the afternoon (1200–1600 LST). However, the maximum magnitude of ΔSST during the afternoon is a factor of two higher during fall (~-0.14°C) than summer (~-0.07°C). Analysis based on observations and ACP sensitivity experiments indicates that the shallow daytime thermocline and associated thin surface ML is the primary factor regulating the day to night difference in ΔSST associated with ACPs. The presence of this shallow daytime thermocline and thin ML amplifies the effects on SST of net surface heat loss and entrainment of cold sub-surface water associated with enhanced ACP wind speeds.

Plain Language Summary Atmospheric cold pools (ACPs) generated from convective systems can significantly modulate air-sea interaction processes over the ocean. However, the modulation of sea surface temperature (SST) in response to intense air-sea interaction processes associated with ACPs is not yet documented in the Bay of Bengal (BoB). Our analysis based on high-temporal resolution moored buoy observations reveals a well-defined diurnal variability in the reduction of SST with an afternoon peak due to ACP activity in the BoB. One-dimensional mixed layer (ML) model sensitivity experiments suggest that the formation of the daytime thermocline and associated thin ML is the primary factor determining the enhanced reduction in SST during the afternoon compared to the night. The presence of this shallow daytime thermocline and thin ML amplifies the effects on SST of net surface heat loss and entrainment of cold sub-surface water associated with enhanced ACP wind speeds. The present study highlight that it is imperative to accurately represent ACP activity and associated air-sea interaction processes in the coupled model using for seasonal weather predictions.

1. Introduction

Sea surface temperature (SST) in the Bay of Bengal (BoB) varies across a wide range of temporal scales from diurnal to interannual, and these variations play a vital role in determining the seasonal variation of monsoon precipitation over land (Jiang & Li, 2011; Roxy & Tanimoto; 2007; Samanta et al., 2018; Shankar et al., 2007; Shenoi et al., 2002). SST variability on diurnal time scales is one of the most critical components in the climate system, and this variation is primarily modulated by the diurnal cycle of solar insolation (Anderson & Riser, 2014; Bernie et al., 2005; Mujumdar et al., 2011; Shenoi et al., 2009; Shinoda, 2005; Thushara & Vinayachandran, 2014). In addition, the generation of near-surface turbulence associated with the formation of a diurnal jet due to the trapping of wind momentum in the near-surface layer can also modulate the diurnal variability of SST (Sutherland et al., 2016; Wenegrat & McPhaden, 2015).

Previous studies have shown that diurnal changes in SST help to precondition the atmosphere for deep convection in the active rainfall phase of tropical intraseasonal variations (Johnson & Ciesielski, 2017; Johnson et al., 1999; Ruppert & Johnson, 2016; Seo et al., 2014; Slingo et al., 2003; Webster et al., 1996). Hence,

improved knowledge of sub-daily variability in air-sea fluxes and its impact on the diurnal modulation of SST may help with the accurate representation of diurnal scale coupling between the ocean and atmosphere in climate prediction models used for seasonal and extended range monsoon prediction (Bernie et al., 2005; Li et al., 2013; Mujumdar et al., 2011; Seo et al., 2014).

SST variations in response to intense air-sea interaction processes associated with atmospheric cold pools (ACPs) are of growing interest, but our understanding is still limited (Anderson & Riser, 2014; de Szoeke et al., 2017; Pei et al., 2018). Using high vertical resolution temperature (∼10 cm) measurements in the near-surface layer, Anderson and Riser (2014) reported a reduction in the upper-layer temperature of the magnitude of ∼0.1°C in response to rainfall events in the tropical western pacific. Using observations and models, Pei et al. (2018) showed that the SST drop due to an ACP in the western equatorial Indian Ocean was primarily associated with a net surface heat flux (NHF) from the ocean to the atmosphere in a shallow precipitation-induced near-surface fresh pool.

However, these earlier studies were based primarily on limited data collected during individual scientific cruises. Using moored buoy data in the central BoB, Jofia et al. (2021) examined the seasonal and diurnal variability of ACP events and found that ACP events are plentiful during summer (May–September) and fall (October–November). In addition, their study also demonstrated that diurnal variability of ACP events in the BoB during the summer occurred in association with the sub-daily evolution of southeastward propagating synoptic-scale rainfall anomalies in the BoB, such that the events are more frequent and intense during the afternoon (1200–1800 LST). On the other hand, they found no diurnal variability in ACP events during fall.

The intense air-sea interaction processes associated with the ACPs in the BoB presumably influence SST in this region (Jofia et al., 2021). Our purpose here is to examine whether SST drops in response to ACPs in the BoB during summer and fall show any diurnal variability. If so, what are the causative mechanisms responsible for this diurnal variability, and what is the magnitude of the SST response to the ACPs? To answer these questions, we use Research Moored Array for African-Asian-Australian Monsoon Analysis and Prediction (RAMA) buoy data with 10-min temporal resolution at 8°, 12°, and 15°N along 90°E (Figure 1) in the central BoB (McPhaden et al., 2009). These same data were also used in the ACP study of Jofia et al. (2021). In addition, we use the Price, Weller, and Pinkel (PWP) mixed layer (ML) model (Price et al., 1986) to explore the mechanisms responsible for observed changes in ML properties.

To illustrate the impact of ACP events on SST, Figure 2 shows the time series of high temporal resolution air temperature, NHF, and SST obtained from the RAMA mooring at 15°N, 90°E on July 16, 2009. In response to an ACP event, as evident in the reduction in air temperature and NHF, SST shows a sudden decrease with a magnitude of 0.07°C (Figure 2). Such variations in SST are the primary focus of our study. Note that in response to the ACP event, SST decreases much faster than the average diurnal cycle (Figure 2), indicating that ACPs can significantly modulate the diurnal evolution of SST.

The study is organized as follows. In Section 2, we describe the data sets, methodology, and PWP model experiments. In Section 3, we investigate the diurnal variability in the reduction of SST due to ACP events and the causative mechanisms responsible for this variability. Major results are summarized in Section 4.

2. Data and Methods

2.1. Data

Meteorological measurements from the RAMA moorings were made at 3–4 m above sea level, including the downwelling shortwave and longwave radiation, wind velocity, air temperature, and relative humidity. In addition, RAMA moorings measure ocean temperature at depths of 1 (nominally defined as SST), 5, 10, 20, 40, 60, 80, and 100 m with 10-min sampling interval and salinity at depths of 1 (nominally defined as sea surface salinity), 10, 20, 40, 60, and 100 m with 1-h sampling interval.

The downwelling shortwave flux observations from the mooring were corrected for an albedo of 6% to estimate net surface shortwave radiation (NSW). The downwelling longwave radiation obtained from the RAMA moorings was adjusted for black body radiation from the sea surface to estimate net longwave radiation (NLW). Latent heat flux (LHF) and sensible heat flux (SHF) were estimated with the Coupled
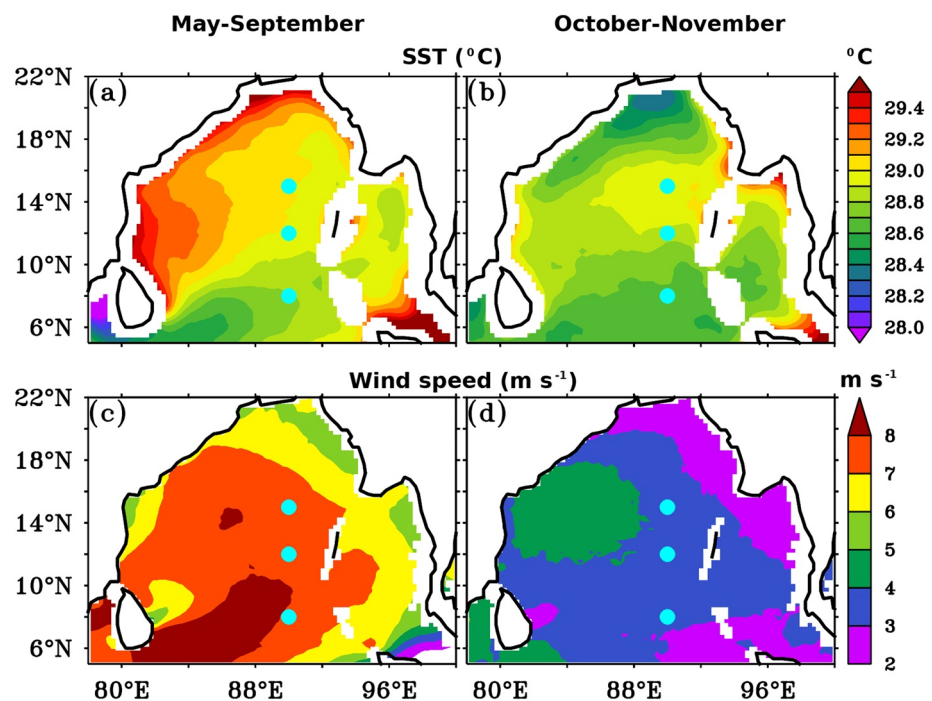
Figure 1. The seasonal average (a and b) of optimally interpolated microwave SST (°C) at 25 km horizontal resolution and (c and d) ASCAT wind speed (m s⁻¹) with 25 km resolution during (a and c) summer (May–September) and (b and d) fall (October–November) in the Bay of Bengal (BoB). The RAMA mooring locations in the BoB are marked in cyan circles.

Ocean-Atmosphere Response Experiment (COARE 3.6) bulk flux algorithm (Edson et al., 2013; Fairall et al., 2003) using mooring SST, air temperature, relative humidity, downwelling shortwave, and downwelling longwave radiation. The NHF is the sum of NSW, NLW, LHF, and SHF.

Note that downwelling longwave radiation sensors were not deployed on the RAMA moorings at 12° and 8°N; hence, Clouds and the Earth's Radiant Energy System (CERES) hourly downwelling longwave radiation data with 1° × 1° spatial resolution (Wielicki et al., 1996) was used to estimate LHF and SHF and also to calculate NHF. We tested the sensitivity of using the hourly CERES data instead of 10-min RAMA downwelling longwave radiation at 15°N in computing the diurnal variations in the NHF. For this purpose, we interpolated hourly downwelling longwave radiation data to the temporal resolution of RAMA downwelling longwave radiation. The Root Mean Square Difference (RMSD) of NHF between these two estimates during summer and fall is ∼10 W m⁻². These differences are generally small relative to the diurnal amplitude of the NHF variations (standard deviation is ∼280 W m⁻²) observed in the BoB. Similarly, during summer and fall, the RMSD between LHF estimates based on CERES and RAMA downwelling longwave radiation data is ∼0.5 W m⁻², while those for SHF are ∼0.1 W m⁻². Thus, the above analysis indicates that using CERES downwelling longwave radiation data instead of 10-min RAMA data provides reasonable estimates of diurnal variation of NHF at 12° and 8°N.

Following Yokoi et al. (2014) and Jofia et al. (2021), an ACP event is identified as when the air temperature drops by at least 1°C within 30 min. The active duration of an ACP event is considered as the period between when air temperature starts to decrease (T_{intial}) and when it reaches the minimum value (T_{final}; Figure S1). The intensity of the ACP event is defined as the difference in air temperature (ΔT_a) at T_{intial} and T_{final}. The responses of other parameters (e.g., ΔSST) to the ACP event are estimated as the difference between T_{final} minus T_{intial} values.

Following Jofia et al. (2021), ACP events are categorized into single, double, and multiple according to their frequency of occurrence. Events separated by 4 h are considered as a single events; if two consecutive events occur in less than 4-h, they are considered as a double event; if more than two events occur successively in
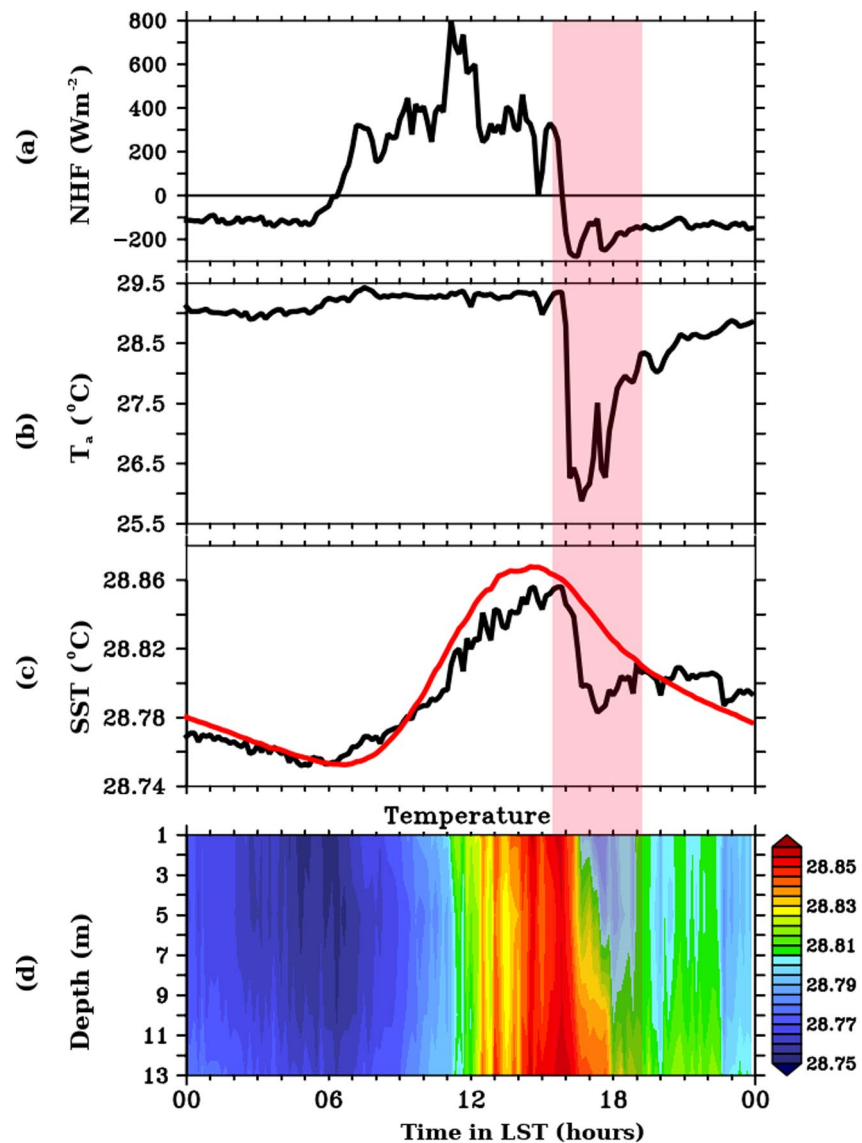
Figure 2. The sub-daily evolution of (a) Net surface heat flux (W m^{-2}), (b) air temperature (°C; T_a), (c) Sea surface temperature (SST) (°C; black line), and (d) vertical profile of temperature (°C) from RAMA mooring at 15°N, 90°E on July 16, 2009. The red transparent vertical shading represents an atmospheric cold pool event. The red line in panel (c) represents the diurnal evolution of the composite of SST anomalies (daily mean is removed from each day) at 15°N, 90°E during summer. The composite diurnal cycle of SST is reduced by a factor of 2 and adjusted to a mean of 28.8°C for the comparison of SST values on July 16, 2009. Time in LST (h).

less than 4-h, they are considered as a multiple events. The total and single ACP events identified during fall and summer of the study period are presented in Table 1. Of all the ACP events identified during fall and summer, ~70% of events were single (Table 1). Hence, the analysis based on the ACP category single events alone can provide statistically reliable information on the impact of ACP events on SST. Hence, following Jofia et al. (2021), our discussion will focus on single events for the sake of brevity. The analysis is based on four (2009, 2013, 2014, and 2015), six (2010, 2011, 2012, 2013, 2014, and 2015), and two (2008 and 2011) years at 15°, 12°, and 8°N, respectively.

Optimal interpolated microwave SST at 25 km horizontal resolution (Gentemann et al., 2004) and the daily average of the Cross-Calibrated Multi-Platform (CCMP) version 2 gridded surface vector winds (Atlas et al., 2011) with 0.25° spatial resolution are used to describe the prevailing SST and wind speed conditions in the BoB during summer and fall.

Table 1

The Number of Single, Double, and Multiple ACP Events Observed at 15°, 12°, and 8°N in the Bay of Bengal During the Summer (May–September) and Fall (October–December)

Cold pool events	15°N	12°N	8°N
Summer			
Single	436 (68%)	418 (67%)	347 (70%)
Double	139 (21%)	129 (20%)	88 (18%)
Multiple	76 (11%)	87 (13%)	59 (12%)
Fall			
Single	164 (73%)	175 (68%)	219 (72%)
Double	40 (18%)	53 (21%)	54 (18%)
Multiple	20 (9%)	28 (11%)	30 (10%)

Note. The percentage of occurrence of atmospheric cold pool (ACP) events in each category based on the total events observed at respective mooring locations are presented in the brackets.

In this study, all the data are presented in Local Sidereal Time (LST; 5 h 30 min ahead of UTC). The daily average from the particular day (defined as 24 h from 0600 LST) is removed to estimate daily anomalies. The diurnal range of a parameter is defined as the difference between the maximum and minimum values in a day (Clayson & Weitlich, 2007; Cronin & McPhaden, 1999). For ease of interpretation, only the composite evolution of meteorological and oceanographic parameters is presented in the study. The uncertainty of the mean is presented as one standard error and is estimated using bootstrap methods.

Note that the definition of summer (May–September) and fall (October–November) used in this study departs from the standard definition of June–August and September–October, respectively, though it is consistent with the previous study of ACPs in the BoB by Jofia et al. (2021). In their study, the definition of summer and fall was primarily chosen based on the seasonal variability of wind velocity in the BoB (Figure S2). The seasonal evolution of climatological wind speed and vectors in the BoB shows the existence of southwesterly winds with a magnitude greater than 5 m s⁻¹ from May to September during the southwest monsoon and relatively weak wind speed conditions (<3 m s⁻¹) during October–November transition between the southwest and northeast monsoon.

Alternatively, one can think of these seasons as the Indian summer monsoon and the monsoon transition seasons.

The role of pre-existing hydrographic conditions on ACP induced SST cooling is qualitatively examined using Equations 1 and 2 below. The potential energy of the water column from the surface to an ML depth of h (PE_h) is estimated through the following equation

$$PE_h = g \int_h^0 \overline{\rho(h)} h \, dh = 0.5 g \overline{\rho(h)} h^2, \tag{1}$$

where g is the acceleration due to gravity (9.8 m s⁻²), ρ is the potential density and $\overline{\rho(h)}$ is potential density averaged over the depth h (m).

The rate of change of ML (h) temperature (T_h) due to NHF and entrainment processes is estimated through

$$\frac{\partial T_h}{\partial t} = \frac{NHF - Q_{pen}}{\rho C_p h} - \frac{\partial h}{\partial t} \frac{(T_h - T_{\Delta h})}{h}, \tag{2}$$

where the terms from left to right represents temperature tendency, temperature change due to NHF, and entrainment cooling due to deepening of the ML (Girishkumar et al., 2017). In Equation 2, $\partial h / \partial t$ is entrainment velocity due to deepening of the ML, C_p is the specific heat capacity of seawater (4,000 J Kg⁻¹ K⁻¹), ρ is the density of seawater (1,024 kg m⁻³), T_h is temperature averaged over h, $T_{\Delta h}$ is the temperature at the base of the ML and ($T_h - T_{\Delta h}$) is the temperature gradient at the base of the ML. Q_{pen} is shortwave radiation penetrating below the ML.

2.2. PWP Model

We use data from the 15°N, 90°E RAMA site for experiments with PWP model primarily due to the availability of all the components of NHF at this location. The PWP model is initialized with the temperature and salinity profiles with a 2-m vertical resolution obtained from the Argo float (WMOID 2901333) located nearest to the mooring at 14.247°N, 89.038°E on May 16, 2013 (Figure S3). High-vertical resolution Argo data provides a better initial condition of stratification below the ML, and this is the primary motivation to use data from the float rather than the mooring to initialize the model. Note that the Argo float temperature data shows a slightly higher value than RAMA, probably because the float is located ~100 km away from the mooring at 15°N, 90°E. Using a simple linear regression between data from Argo and RAMA, the offset in the Argo temperature measurement is corrected, and the corrected float data is used to initialize the PWP

model (Figure S3). We used 1 m vertical grid resolution with a maximum depth of 100 m for the model simulation and a time step of 600 s (10 min). The PWP model experiments used in this study are summarized in Table 2 and described in more detail in Section 3.2.1.

Following Paulson and Simpson (1977), the Q_{pen} in the model water column is parameterized by the expression

$$Q_{pen} = NSW\left[Re^{z/\zeta_1} + \left(1 - R\right)e^{z/\zeta_2} \right], \tag{3}$$

where z is depth in m, ζ_1 is the attenuation depth (m) of the infrared and red part of shortwave radiation, and ζ_2 is the attenuation depth of the remaining part of shortwave radiation. Constant values 0.62, 0.6, and 20 m were used for parameters R, ζ_1, and ζ_2, respectively, and this selection is based on Jerlov (1968) type 1A water classification, representing typical open ocean conditions in the BoB (Babu et al., 2004; Kantha et al., 2019). However, different values for ζ_1 (0.6–1.5 m) have been used in the previous studies in the BoB (Babu et al., 2004; Buckley et al., 2019; Lotliker et al., 2016). Note that the infrared and red parts of the spectrum are typically absorbed in the upper 2–3 m of the water column, and a value of 0.6 and 1.5 m for ζ_1 leads to absorption of 95% of the infrared-red parts of the spectrum in the upper 2 and 4 m of the model water column, respectively. These characteristics suggest that the selection of value 0.6 m for ζ_1 does not significantly influence the model simulation. A recent study based on the *in situ* observations of hyperspectral downwelling irradiance in the visible spectrum in the BoB (<15°N) during summer reported a value of 19 ± 3 m for ζ_2 (Table 1 of Lotliker et al., 2016), which is close to the model parameter used in the study. In addition, ζ_2 estimated by an 8-days composite of chlorophyll data at a spatial resolution of 5 km from Moderate Resolution Imaging Spectroradiometer (MODIS) onboard Aqua satellite from January 2003 to March 2020 using the expression ($\zeta_2 = [0.027 + 0.0518*$ chlorophyll$^{0.428}]^{-1}$) proposed by Morel (1988) shows a mean value around 19.9 ± 0.02 m at 15°N, 90°E in the BoB. The choice of these parameters is important to accurately simulate SST in an ocean model (Buckley et al., 2019; Kantha et al., 2019). However, the main goal of our study is to explore the sensitivity for SST responses to ACPs under different initial conditions and forcing scenarios, so the exact choice of parameters to estimate the Q_{pen} in the model is not critical to understanding our results.

Due to the absence of horizontal and vertical advection in Equation 2 and uncertainty in estimating Q_{pen} in the water column, we do not expect the PWP CTRL run to fully simulate temperature and salinity changes as observed in the in-situ data. For example, Buckley et al. (2019) discussed the importance of horizontal freshwater and heat advection in simulating seasonal variability of sea surface salinity and SST. However, we hope to gain some physical insight on how one-dimensional processes operate on the short time scale of ACP events to impact SST.

3. Results

### 3.1. Observation of Impact of ACP Events on SST

The existence of diurnal variability of the magnitude of SST cooling due to the ACP events during summer and fall at the mooring locations is evaluated through a composite evolution of observed ΔSST (Figures 3b and 4b; black line). A well-defined diurnal variability of ΔSST due to ACP events, with an afternoon peak, is apparent during summer and fall at all RAMA sites in the BoB, such that the ΔSST values progressively increase from 0800 to 1000 LST and reach a maximum value around 1400–1500 LST (Figures 3b and 4b). They then decrease afterward, reaching a minimum value (−0.02°C) around 0400–0600 LST (Figures 3b and 4b). It is important to note that the magnitude of ΔSST during the afternoon is a factor of two higher during fall (−0.14°C) than summer (∼−0.07°C; cf. Figures 3b and 4b).

The percentage of occurrence of different magnitudes of the SST drop (ΔSST) due to ACP events during the summer shows that the bulk (∼45%) of the reduction is smaller than −0.02°C (Figures 5a–5c). During summer, at 15° and 12°N, the average magnitude of ΔSST is higher than (−0.04°C) at 8°N (−0.02°C), and the ΔSST associated with individual ACP events reaches as much as −0.16°C (Figures 5a–5c). Note that at 15° and 12°N, ∼20% of ACP events have a ΔSST of more than −0.05°C during summer (Figures 5a–5c). However, while considering the events that occurred between 1000 and 1800 LST during summer, ∼25% of ACP events have a ΔSST of more than −0.05°C at 15° and 12°N (Figure not shown).

Table 2
List of All the Price, Weller, and Pinkel (PWP) Control Run and Atmospheric Cold Pool (ACP) Experiments

Experiment name	Characteristics of the model run	Purpose of the model run
Control run		
CTRL	Control model run based on the observed meteorological fields.	To evaluate the PWP model performance at the study region.
WW_CTRL	The fourth-day average values for all the parameters in the CTRL run forcing field used, except for NSW (3-h running mean is applied) and wind stress (τ) (prescribed as zero). WW designates "without wind stress forcing"	To isolate the impact of the high-frequency diurnal variability of momentum, radiative, and turbulent heat fluxes on SST.
WW_CTRL_2 m	Similar to WW_CTRL; but model vertical resolution changed from 1 to 2 m	To test the sensitivity of model vertical resolution on ΔSST due to ACP events.
WW_CTRL_6 m	Similar to WW_CTRL; but model vertical resolution changed from 1 to 6 m	
ACP run		
CP_CTRL	ACP forcing field prescribed on the top of CTRL forcing field.	To simulate diurnal variability of ΔSST due to ACP.
CP_WW_CTRL	ACP forcing field prescribed on the top of WW_CTRL forcing field.	
ACP sensitivity test during the night		
CP_WW_CTRL_2τ	Wind stress (τ) in the ACP forcing field increased from 0 to 0.25 N m^{-2}.	To test the sensitivity of ΔSST to wind stress (τ) enhancement during ACP events.
CP_WW_CTRL_2NHF	NHF loss in the ACP forcing field increased from -150 to -350 W m^{-2}.	To test the sensitivity of ΔSST to the enhancement of NHF during ACP events.
CP_WW_CTRL_3NHF	NHF loss in the ACP forcing field increased from -150 to -450 W m^{-2}.	To test the sensitivity of ΔSST to the enhancement of NHF during ACP events.
CP_WW_CTRL_2NHF_3P	NHF loss was increased from -150 to -350 W m^{-2} and the precipitation rate (P) increased from 0 to 18 mm h^{-1} in the ACP forcing field.	To test the sensitivity of ΔSST to the enhancement of near-surface stratification and SHF associated with the precipitation during ACP events.
CP_WW_CTRL_3NHF_3P	NHF loss increased from -150 to -450 W m^{-2} and the precipitation rate (P) increased from 0 to 18 mm h^{-1} in the ACP forcing field.	
ACP sensitivity test based on the strength of daytime thermocline		
20NSW_WW_CTRL	20% reduction applied to fourth-day NSW forcing field of WW_CTRL run.	To create different realizations of the shallow daytime thermocline with respect to WW_CTRL run.
40NSW_WW_CTRL	40% reduction applied to fourth-day NSW forcing field of WW_CTRL run.	
60NSW_WW_CTRL	60% reduction applied to fourth-day NSW forcing field of WW_CTRL run.	
CP_20NSW_WW_CTRL	ACP forcing field prescribed on the top of 20NSW_WW_CTRL forcing field.	To test the sensitivity of ΔSST to the strength of the daytime thermocline during ACP events.
CP_40NSW_WW_CTRL	ACP forcing field prescribed on the top of 40NSW_WW_CTRL forcing field.	
CP_60NSW_WW_CTRL	ACP forcing field prescribed on the top of 60NSW_WW_CTRL forcing field.	
ACP sensitivity test based on the model vertical resolution		
CP_WW_CTRL_2 m	Similar to CP_WW_CTRL; but model vertical resolution decreased from 1 to 2 m.	To test the sensitivity of model vertical resolution on ΔSST due to ACP events.
CP_WW_CTRL_6 m	Similar to CP_WW_CTRL; but model vertical resolution decreased from 1 to 6 m.	
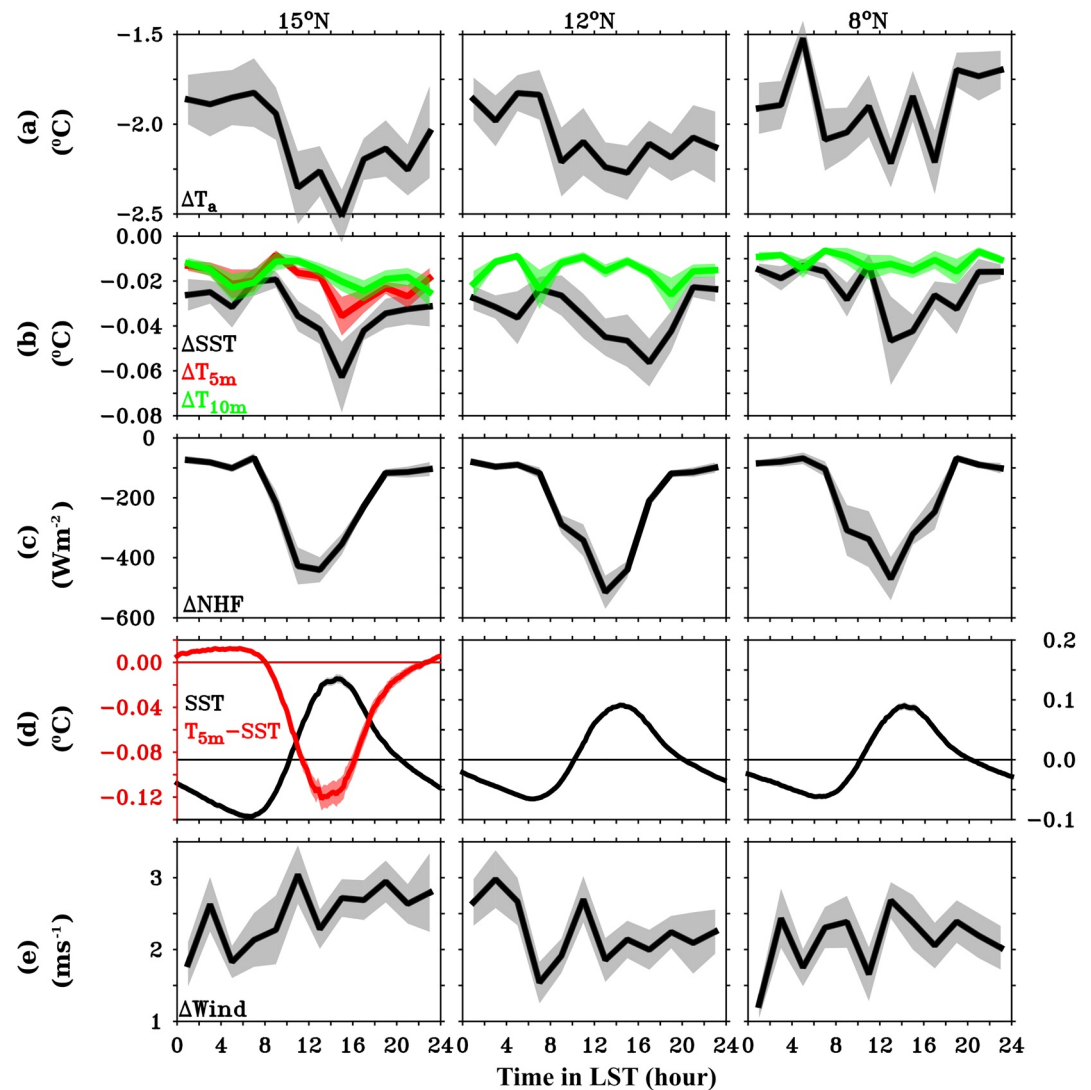
Figure 3. The diurnal variability of (a) reduction in air temperature (°C; ΔT_a), (b) reduction in water temperature (°C) at 1 m (ΔSST; black line), 5 m (ΔT_{5m}; red line) and 10 m (°C; ΔT_{10m}; green line), (c) reduction in net surface heat flux (NHF) (W m^{-2}; ΔNHF), and (e) enhancement of wind speed (m s^{-1}; ΔWS) due to single atmospheric cold pool (ACP) events with respect to pre-ACP conditions averaged over 2-h bins derived from the RAMA mooring locations at (left) 15°N, 90°E; (middle) 12°N, 90°E; and (right) 8°N, 90°E during summer. The 2-h averaged values are centered at the middle of each 2-h period; for instance, ΔSST corresponding to 0500 LST represents the average value between 0400 and 0559 LST. (d) The climatology of diurnal variability of SST anomaly (°C; after removing the daily mean from corresponding days; black line) and the temperature difference (°C; red line) between 5 and 1 m derived from the RAMA mooring location at (left) 15°N, 90°E; (middle) 12°N, 90°E; and (right) 8°N, 90°E during summer. Shading represents the one-standard error, and it is estimated based on the deviations of data from the mean in each 2-h bins. Time in LST hours.

During fall, the frequency distribution of ΔSST due to ACP events shows that ~40% of the reduction is smaller than −0.02°C, and about 32% of ACP events have ΔSST of more than −0.05°C (Figures 5d–5f). The ΔSST associated with individual ACP events reaches as much as −0.3°C with an average drop of around −0.07°C during fall (Figures 5d–5f). Moreover, the events that occurred between 1000 and 1800 LST during fall, ~45% of ACP events have ΔSST of more than −0.05°C (Figure not shown), and the average drop is higher (−0.1°C) than the total events at 15° and 8°N. Note that the difference in the magnitude of ΔSST due to the ACP between fall and summer is noticeable only during the 1000–1800 LST (Figures 3b and 4b). These characteristics suggest that between 1000 and 1800 LST, the ACP events during fall tend to generate
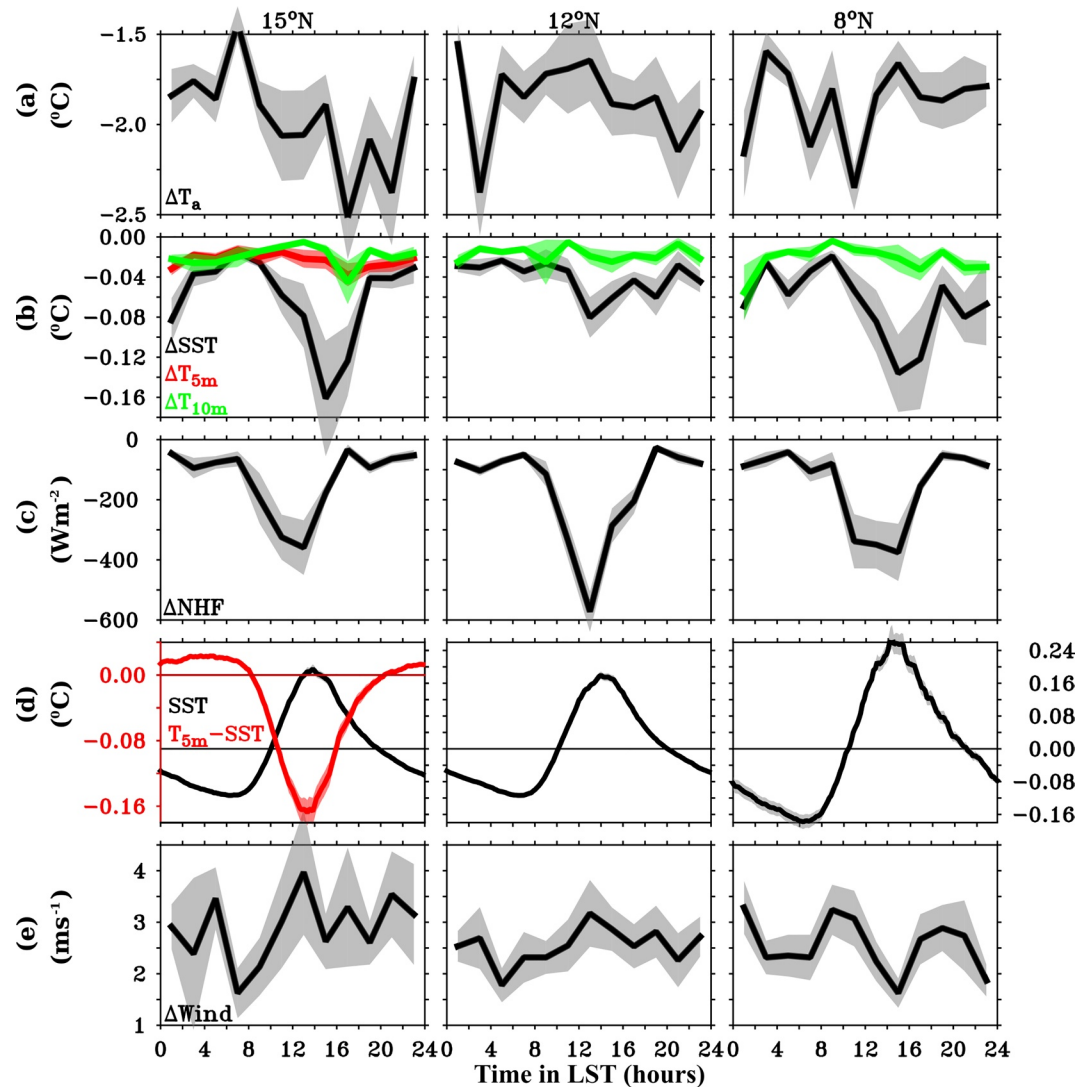
Figure 4. Same as Figure 3 in the manuscript but for fall. Note that the *y*-axis limits in panels (b), (d), and (e) are different compared to Figure 3.

relatively more SST cooling than the events that occur during summer. Note that ~40% (33%) of events at 15° and 12°N (8°N) during summer and ~32% of events during fall occur between 1000 and 1800 LST.

The diurnal variability of reduction in the water temperature at 5 m depth ($\Delta T_{5\,m}$) and 10 m depth ($\Delta T_{10\,m}$) during summer and fall are examined to understand how deep the cooling tendency associated with the ACP penetrates (Figures 3b and 4b; red and green lines). The $\Delta T_{10\,m}$ shows an average drop of around −0.015°C and does not show the signature of diurnal variability (Figures 3b and 4b; green line). However, at 15°N, the $\Delta T_{5\,m}$ shows similar diurnal variation as observed in ΔSST, though the magnitude of the former is less than the latter by a factor of 2, particularly between 1200 and 1800 LST (Figures 3b and 4b; red line). This characteristic suggests that the reduction in ocean temperature in response to ACP events in the BoB is typically restricted to the upper 10 m of the water column. This feature is consistent with an earlier study (Anderson & Riser, 2014). Using the high vertical resolution of temperature measurements from a profiling float in the western pacific, Anderson and Riser (2014) show that reduction in ocean temperature (~0.1°C) restricted to the upper 6–8 m of the water column in response to a single convective event, which is similar to our observations in the BoB.
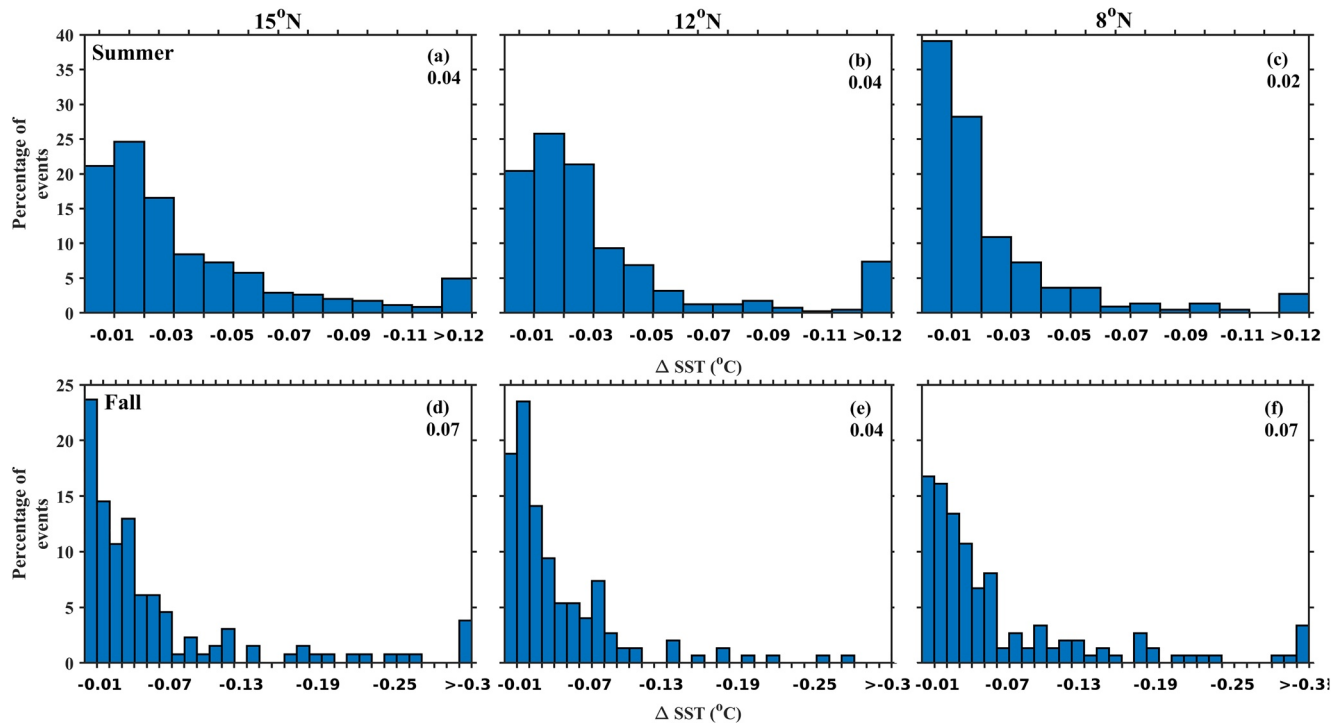
Figure 5. The frequency of sea surface temperature (SST) drop (°C; ΔSST) in 0.01°C bins (e.g., −0.01°C ΔSST corresponds to the percentage of events with SST drop between 0 and −0.01°C) during (a–c) summer and (d–f) fall due to the single ACP events at (left) 15°N, 90°E; (middle) 12°N, 90°E; and (right) 8°N, 90°E. The numbers in the top and bottom panels represent the mean of ΔSST (°C). Note that the upper limit of bins is >0.12°C for summer and >0.3°C for fall.

Note that the magnitude of ΔSST in response to the ACP events is higher than the accuracy of temperature sensors in the RAMA mooring (±0.002°C). The mean diurnal range of SST at the RAMA mooring locations in the BoB is ∼0.20°C, and 0.35°C during summer and fall (Figures 3d and 4d; black line). Hence, the magnitude of ΔSST during summer (∼0.07°C) and fall (∼0.14°C) associated with ACP events during the afternoon is about 35% of the climatological mean of the diurnal range of SST in the study region.

Diurnal variability of ΔT_a, a proxy for ACP intensity, and ΔSST due to ACP event forcing show a strong temporal correspondence between them at 15° and 12°N during summer, such as the maximum value of ΔSST coincides with the period of frequent and intense ACP events during the afternoon (Figures 3a and 3b). Hence, we suggest that intense ACP events during the afternoon account for the higher magnitude of ΔSST in the afternoon. Note that the intensity of ACP events does not show any diurnal variability during fall (Jofia et al., 2021; Figure 4a). Nevertheless, a well-defined diurnal variability of ΔSST due to ACP events with an afternoon peak is apparent during the fall at all RAMA sites in the BoB as observed during the summer (Figures 3b and 4b). Moreover, an afternoon peak in ΔSST is also evident during the summer at 8°N in the BoB; the region does not show diurnal variability in the intensity of ACP events (Figure 3b). In addition, the maximum magnitude of ΔSST at 1500 LST due to the ACP lags the maximum value of ΔNHF at 1200 LST by ∼3 h in the mooring observations (Figures 3b, 3c, 4b and 4c). These characteristics suggest that ACP events occurring during the afternoon tend to generate a relatively higher magnitude SST response than the events that occur during the night. The plausible regulating factors that determine the difference in the ACP induced SST variability between day and night are examined in the following section.

3.2. Impact of the ACP to Determine the Diurnal Amplitude of SST Using the PWP Model

Different processes may work in tandem to determine the reduction in SST during the ACP. Turbulent entrainment of cold subsurface water into the near-surface layer due to enhanced wind speeds and heat loss across the sea surface can be effective in cooling SSTs during ACP events. In addition, NHF from the ocean to the atmosphere can reduce SSTs during ACPs. As depicted in Equation 2, the SST cooling due to entrain-

ment processes is determined by the rate of deepening of the ML (entrainment velocity) and temperature gradient at the base of the ML. Besides, Pei et al. (2018) suggest that trapping of NHF loss in a very thin surface freshwater layer formed due to the precipitation associated with an ACP event can also play an important role in determining SST cooling during an event. Because ML depth appears in the denominator of the terms on the right-hand side for Equation 2, it is evident that the effects of entrainment and surface heat fluxes on SST will be amplified during those periods when the ML is thin, for example, in the afternoon. Below, we used the PWP model as a tool to investigate the processes that determine the difference in the magnitude of SST cooling during the ACP between day and night.

3.2.1. ACP Experiments Using the PWP Model

Our approach here is to determine whether the model can reproduce the observed diurnal variability of SST drops associated with ACP events for different initial conditions and forcing scenarios rather than evaluating PWP model performance to simulate individual events such as illustrated in Figure 2. For this purpose, we focus on a period during 16–19 May 2013 without ACP events as a baseline. Another reason for selecting this period for the model run was the availability of Argo float data with 2 m vertical resolution close to the mooring location. The model run during 16–19 May 2013 is defined as the control run (CTRL run). Initially, the PWP model ability to simulate the near-surface temperature and salinity is evaluated after forcing the model with 10-min NSW, NLW, SHF, LHF, freshwater flux (evaporation [E] and precipitation [P]), and wind stress (τ) derived from the RAMA mooring at 15°N during 16–19 May 2013 (Figure 6).

The CTRL run shows reasonably good skill in reproducing the diurnal variability of temperature as a function of depth and time compared to observations from the RAMA mooring (Figures 7a–7d). Particularly the CTRL run reproduced the timing of daytime warming and nighttime cooling, diurnal range of near-surface temperature, and vertical structure of near-surface temperature stratification during the daytime (commonly known as diurnal thermocline, which we refer to as the daytime thermocline in the study) as observed in the RAMA measurements (Figures 7a–7d). The near-surface salinity field in both the CTRL run and observation does not show significant diurnal variability (Figures 7e–7h). It is important to note that the composite of sub-daily evolution of near-surface temperature during the summer and fall shows diurnal variability, though such variability is absent in the salinity field (Figure 8; compare top and bottom panels). This feature suggests that the diurnal variability of near-surface density stratification is primarily determined by diurnal variability of temperature, and the role of salinity is negligibly small on this time scale. Hence, the diurnal variability of salinity was not discussed further in this study.

The CTRL run has cold (∼0.15°C) and fresh (∼0.03 psu) biases compared to the observations during the last day of the model run (Figures 6g and 7), which may be due to the lack of three-dimensional processes like horizontal and vertical advection in the model and also to errors in model parameterization schemes. For instance, the absence of a salinification event (∼0.03 psu) between 1800 and 2400 LST in the CTRL run compared to observations is likely associated with the absence of a horizontal and vertical advection processes in the ocean model (Figures 7f and 7h). Note that the cold bias in the CTRL run is comparable in magnitude to earlier studies based on the PWP model in the BoB (Buckley et al., 2019; Chaudhuri et al., 2019; Navaneeth et al., 2019; Weller et al., 2016)

Multiple ACP experiments were performed to understand the governing mechanisms responsible for the diurnal variability of SST due to ACP events. For this purpose, the composite of meteorological parameters (NSW, NLW, SHF, LHF, E-P, and τ) derived from RAMA mooring at 15°N associated with single ACP events during 1200–1800 LST was used as ACP forcing (Figure S4).

The first ACP experiment was based on the CTRL run, defined as the CP_CTRL experiment (ACP control experiment). The CP_CTRL experiment consists of 24 independent ACP simulations, such that the ACP forcing field prescribed in the independent simulations of the CP_CTRL experiment was separated by 1 h. Note that the values of forcing fields in the CTRL run and independent simulations in the CP_CTRL experiment are similar, except the CTRL run forcing fields were replaced with the ACP forcing fields during the specified time window (Figure S5). For instance, Figure S5 depicts the difference in the forcing field used for CTRL runs for 3 out of the 24 independent simulations in the CP_CTRL experiments during the night (0200 LST), morning (0900 LST), and afternoon (1500 LST). In Figure S5, the CP_CTRL (red line) forcing fields can be seen as a large imposed spike over the CTRL forcing fields (black line).
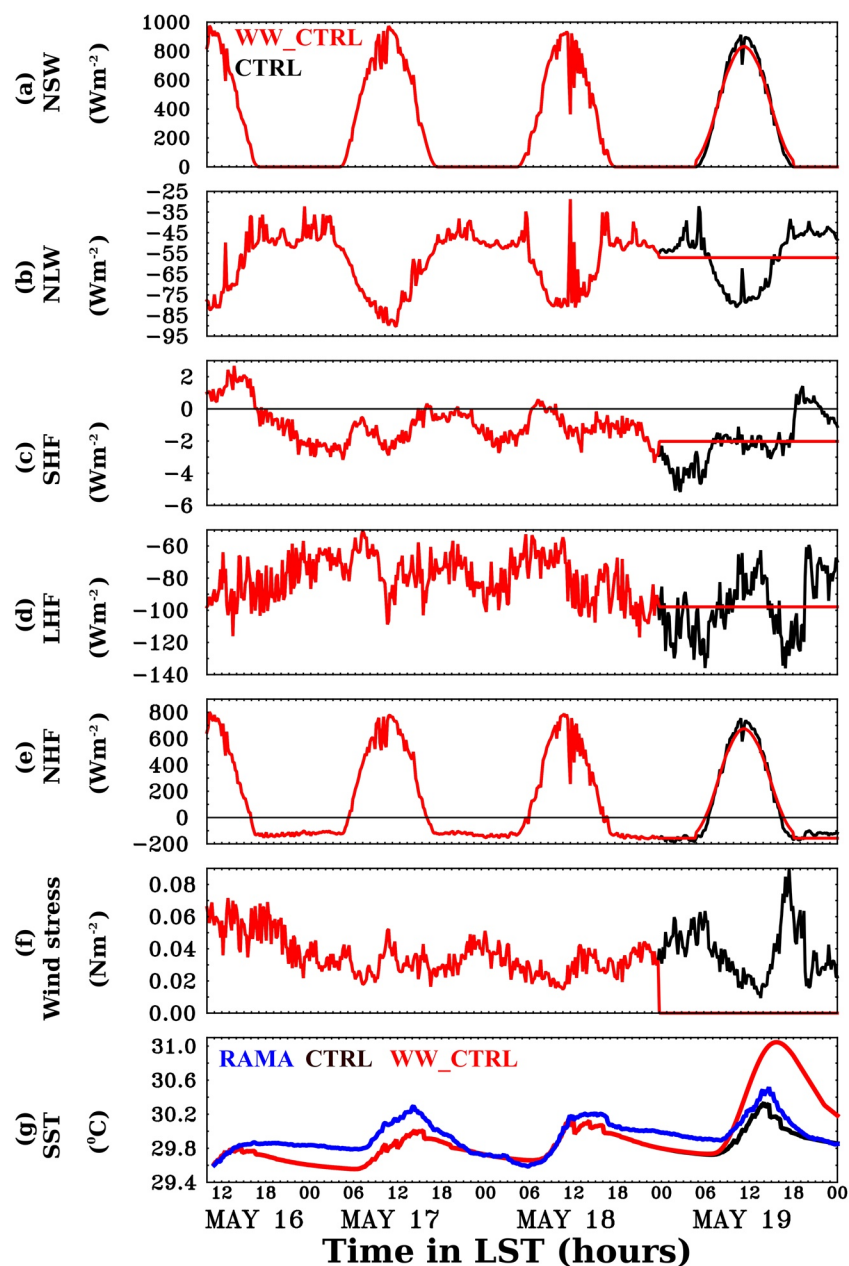
Figure 6. (a) Net shortwave radiation (NSW; W m^{-2}), (b) Net longwave radiation (NLW; W m^{-2}), (c) Sensible heat flux (SHF; W m^{-2}), (d) Latent heat flux (LHF; W m^{-2}), (e) Net surface heat flux (NHF; W m^{-2}) and (f) Wind stress (τ; N m^{-2}) derived from the RAMA mooring at 15°N, 90°E to perform the CTRL (black line) and WW_CTRL (red line) runs for the period during 16–19 May 2013. In the WW_CTRL run, except NSW (a 3-h running mean is applied) and wind stress (prescribed as zero), the fourth-day average values for all the parameters in the CTRL forcing field were used. (g) Temporal evolution of SST (°C) derived from RAMA mooring at 15°N, 90°E (blue), CTRL run (black), and WW_CTRL run (red).

We find that SST simulated in the CTRL run shows intermittent events of mild SST cooling during the daytime warming phase (Figure 9e; black line). Note that such events are also apparent in the observations (Figure S6). This particular characteristic in the model simulated SST field may be associated with turbulent mixing due to the near-surface diurnal jet-induced shear layer (Price et al., 1986; Sutherland et al., 2016; Wenegrat & McPhaden, 2015). As suggested by these studies, the diurnal jet results from the trapping of momentum provided by the wind at the ocean surface in the thin thermally stratified ML during the day-
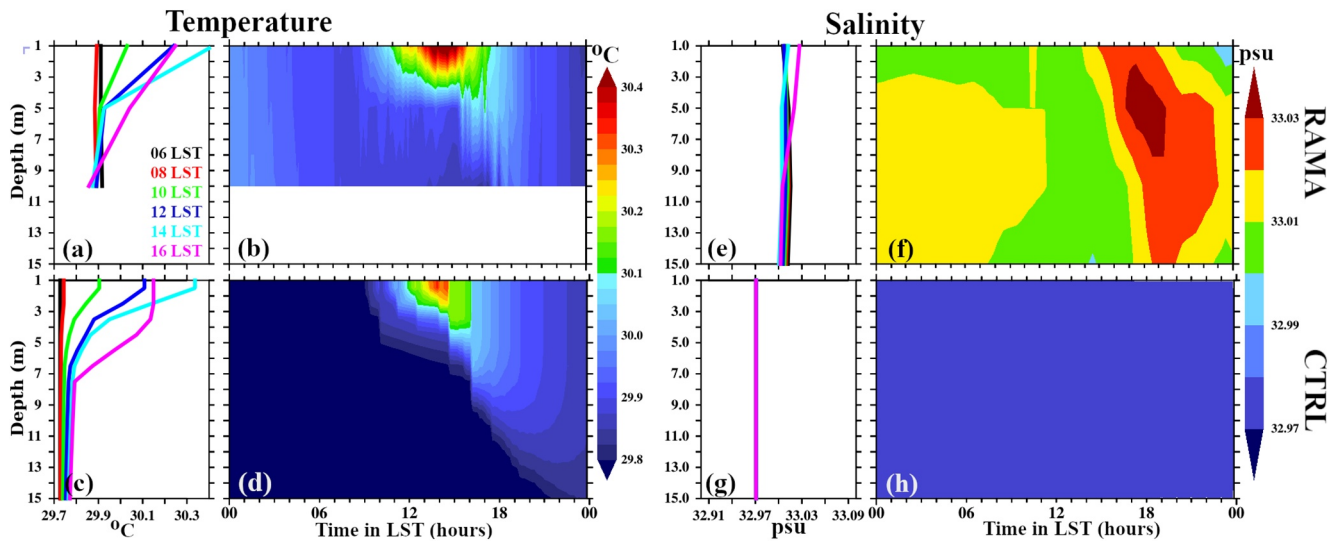
Figure 7. Depth time section (b) Temperature (°C) and (f) Salinity (psu) from RAMA and (d) Temperature (°C) and (h) Salinity (psu) from the CTRL run during 19 May 2019. (a and c) Temperature and (e and g) Salinity profile on 06 LST (black line), 08 LST (red line), 10 LST (green line), 12 LST (blue line), 14 LST (cyan line), and 16 LST (pink line) from (top panel) RAMA and (bottom panel) CTRL run during 19 May 2019. Note that temperature shows apparent diurnal variability in the RAMA and CTRL run, though such a diurnal variability is not evident in the salinity field.

time. One of the main objectives of the present study is to isolate the impact of the ACP on SST. Hence, it is imperative to suppress these dynamical processes associated with the shear layer in the PWP model by removing the momentum forcing field in the CTRL run. The impact of the high-frequency diurnal variability of momentum, radiative, and turbulent fluxes on SST may also lead to difficulty in isolating the SST response due to the ACP from the model experiments.
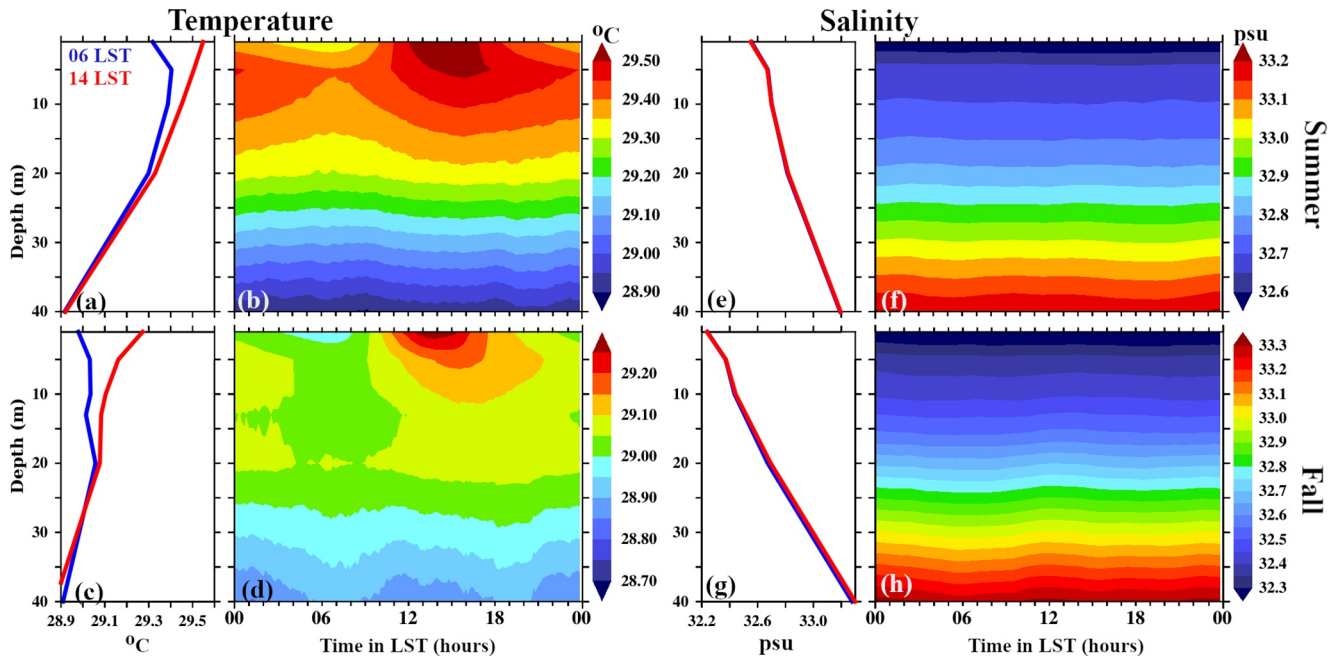
Figure 8. Composite evolution of diurnal variability of the depth-time section of (b and d) Temperature (°C) and (f and h) Salinity (psu) obtained from RAMA mooring at 15°N, 90°E in the Bay of Bengal (BoB) during (top panels) summer and (bottom panels) fall. Composite of (a and c) Temperature and (e and g) Salinity profiles on 0600 LST (blue line) and 1400 LST (red line) obtained from the RAMA mooring at 15°N, 90°E in the BoB during (top panels) summer and (bottom panels) fall.
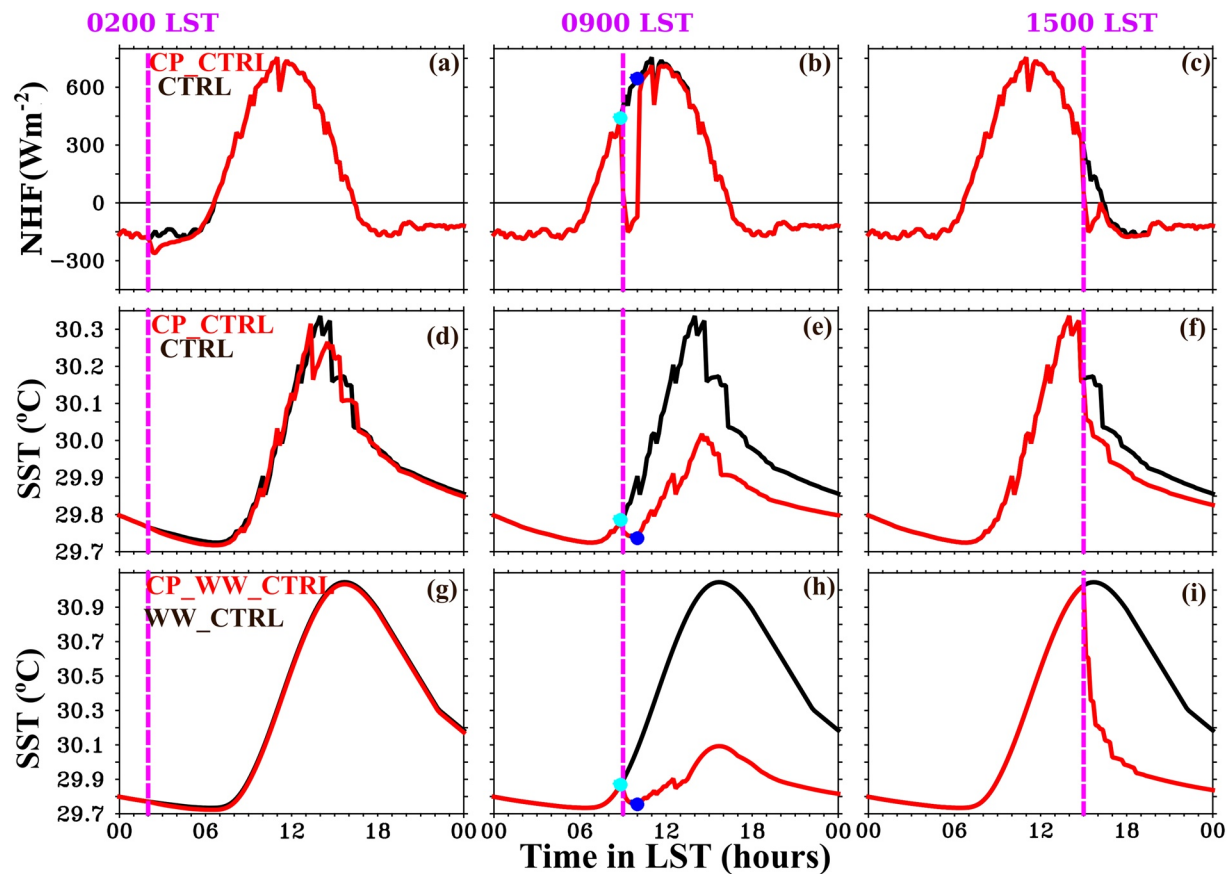
Figure 9. Diurnal variability of sea surface temperature (SST) (°C) simulated by Price, Weller, and Pinkel model (d–f) CTRL (black) and CP_CTRL (red) and (g–i) WW_CTRL (black) and CP_WW_CTRL (red) during three representative time periods (d) and (g) 0200 LST (night), (e) and (h) 0900 LST (morning), and (f) and (i) 1500 LST (afternoon). The top panel represents difference in NHF (W m⁻²) forcing field between CTRL run (black) and CP_CTRL (red) (a) 0200 LST, (b) 0900 LST, and (c) 1500 LST (afternoon). Time in LST (h). The magnitude of SST cooling (ΔSST) in response to CP_CTRL and CP_WW_CTRL experiments on 0900 LST is estimated as the difference in SST just before (cyan dots in panels e and h) and 1 h after prescribing atmospheric cold pool (ACP) forcing field (blue dots in panels e and h). The pink vertical lines represent the ACP forcing field prescribed time. Note that the *y*-axis limit is different between panels (d–f) and (g–i).

Hence, a second control run was performed to simulate a smoothed evolution of near-surface diurnal temperature variability, and it is defined as "*without wind control run*" (WW_CTRL run). In the WW_CTRL run, the fourth-day average values for all the parameters in the CTRL run forcing field were used (Figure 6; red line) except for NSW (3-h running mean is applied) and wind stress (prescribed as zero). The diurnal evolution of SST simulated by the WW_CTRL run shows reasonably good agreement with CTRL run, though the former produces slightly warmer SST (0.6°C) compared to the latter due to the absence of wind-induced vertical mixing (Figure 6g; red line). It is worth noting that the peak value of model-simulated SST is delayed by 1 h in the WW_CTRL run compared to the CTRL run (Figure 6g; compare red and blue line). Moreover, the daytime warming in the near-surface is very strong, and it is restricted to a much shallower layer in the WW_CTRL run than the CTRL run (Figures 10a and 11a). Like the CP_CTRL experiment, 24 independent ACP experiments were performed based on CP_WW_CTRL (Figure S7), and it is defined as a CP_WW_CTRL experiment.

In addition, three more model control runs were conducted, such as 20%, 40%, and 60% reduction was applied in the fourth-day NSW forcing field of WW_CTRL run. These control runs are defined as 20NSW_WW_CTRL, 40NSW_WW_CTRL, and 60NSW_WW_CTRL, respectively. The basic purpose of these three control run was to simulate the different magnitude of the near-surface daytime thermocline (Figure S8). The ACP experiments based on these three CTRL run are defined as CP_20NSW_WW_CTRL, CP_40NSW_WW_CTRL, and CP_60NSW_WW_CTRL (Table 2).
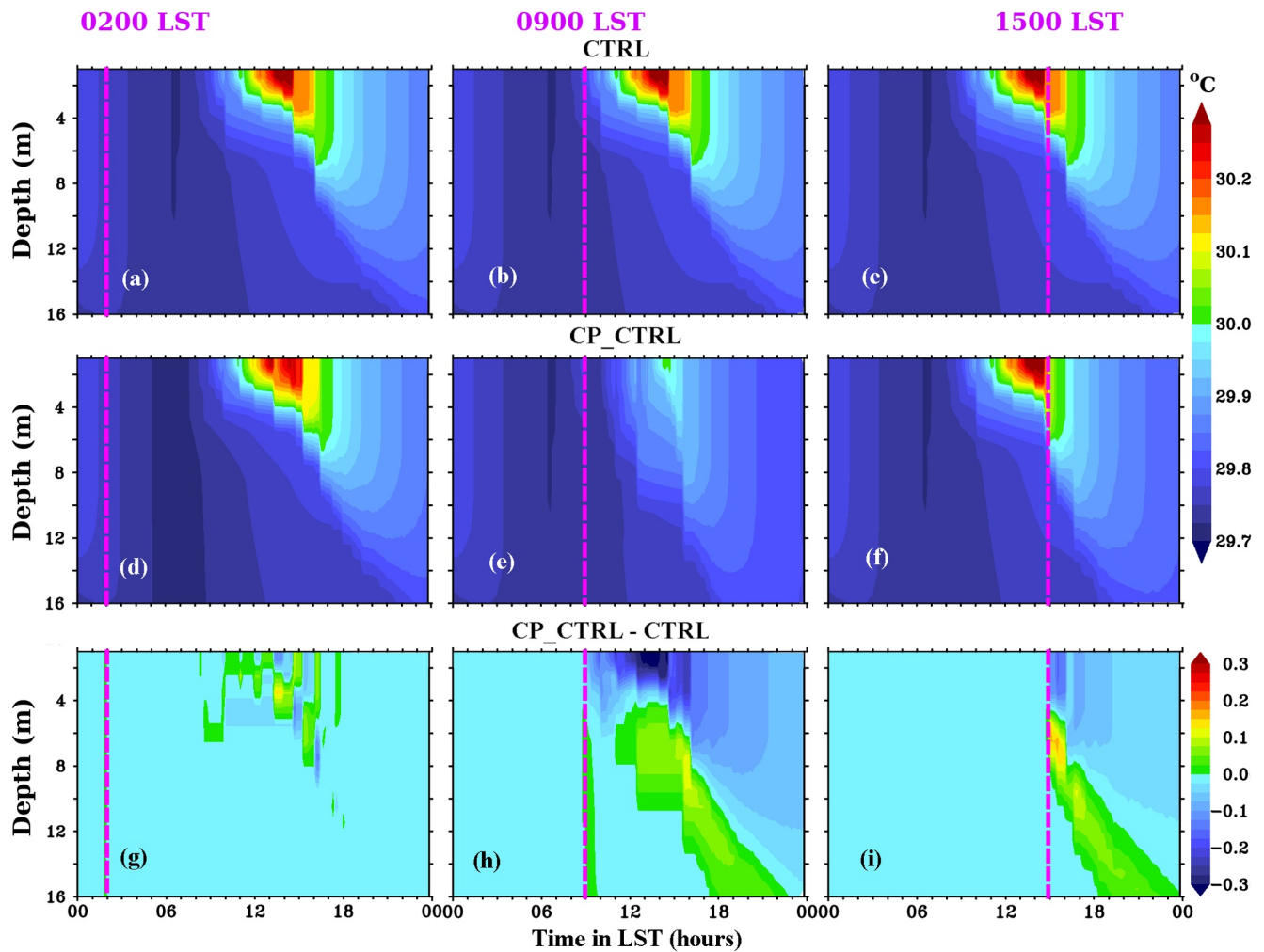
Figure 10. (a–c) Represents diurnal variability in the depth-time section of temperature (°C) simulated in the CTRL run. Diurnal variability in the depth-time section of temperature (°C) simulated by the Price, Weller, and Pinkel model after prescribing atmospheric cold pool (ACP) forcing field (CP_CTRL) instead of CTRL forcing field during three different periods on May 19, 2013 (d) 0200 LST (night), (e) 0900 LST (morning), and (f) 1500 LST (afternoon). The difference between CP_CTRL run and CTRL run on (g) 0200 LST (night), (h) 0900 LST (morning), and (i) 1500 LST (afternoon). Time in LST hours. The pink vertical lines represent the ACP forcing field prescribed time.

When control forcing fields were replaced with ACP forcing fields at a particular time, the magnitude of the forcing fields is similar between the different ACP experiments (CP_CTRL, CP_WW_CTRL, CP_20NSW_WW_CTRL, CP_40NSW_WW_CTRL, and CP_60NSW_WW_CTRL; c.f. red line in Figures S5 and S7). For instance, the magnitude of wind stress (0.14 N m^{-2}) and NHF (-150 W m^{-2}) in the CP_CTRL and CP_WW_CTRL experiment at 0900 LST is the same (Figures S5g and S7g; middle panels).

The ΔSST values in the independent ACP simulation under each experiment (e.g., CP_CTRL, CP_WW_CTRL, and CP_20NSW_WW_CTRL) are estimated as the difference in SST before applying ACP forcing field and 1 h after prescribing ACP forcing field (Figures 9e and 9h; marked as cyan and blue dots). The diurnal variability of ΔSST constructed under each ACP experiment (e.g., CP_CTRL) is evaluated to understand the impact of ACP occurrence time on the magnitude of SST cooling.

3.2.2. Diurnal Variability of ΔSST in ACP Experiments

The diurnal variability of ΔSST and temperature difference between 5 and 1 m estimated from CP_CTRL and CP_WW_CTRL experiments are shown in Figure 12. As in the observations, diurnal variability of ΔSST in the CP_CTRL experiment is apparent, with model simulated ΔSST values progressively increasing from 0800 to 1000 LST (-0.03°C), reaching a maximum value (-0.35°C) around 1300–1400 LST (Figure 12a),
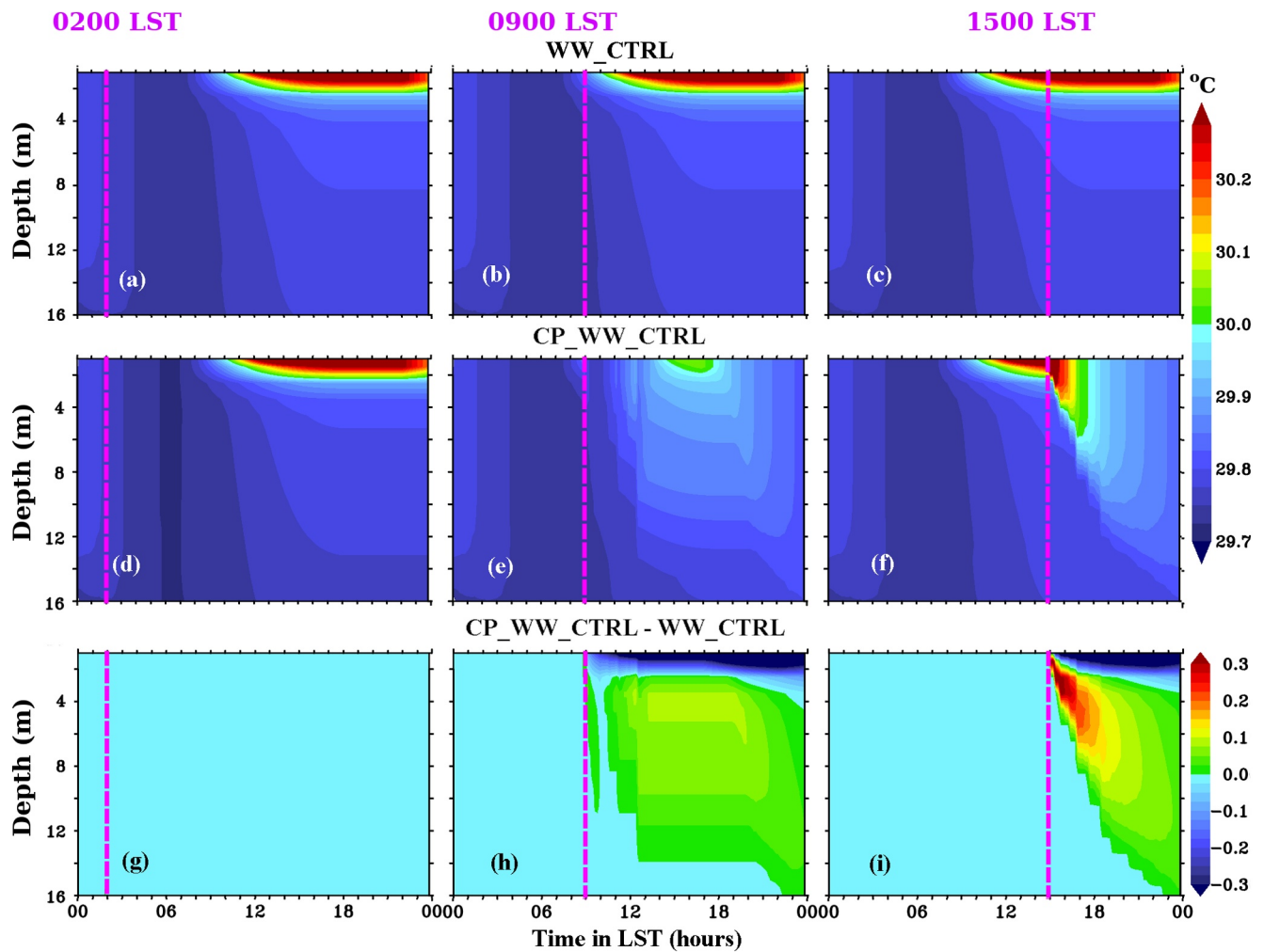
Figure 11. Same as Figure 10, but for (a–c) WW_CTRL, (d–f) CP_WW_CTRL, and (g–f) difference in temperature between CP_WW_CTRL and WW_CTRL.

then decreasing afterward to a minimum value (−0.04°C) around 2300 LST (Figure 12a). Diurnal variability of ΔSST with a slightly higher magnitude than in the CP_CTRL experiment is also apparent in the CP_WW_CTRL experiment. Note that the diurnal range of ΔSST in CP_CTRL and CP_WW_CTRL experiments is higher than in observations (Figures 3b, 4b and 12a), discussed in detail in Section 3.2.4. More importantly, the diurnal variability of ΔSST simulated by CP_CTRL and CP_WW_CTRL experiments shows good temporal correspondence with the observations (Figures 3b, 4b and 12a), which gives us the confidence to use a one-dimensional ML model to examine the physical mechanism that determines the difference in the ACP induced ΔSST magnitude between day and night.

3.2.3. Role of Enhancement of NHF Loss During ACP Events

Variability in NHF (ΔNHF) due to ACP events shows an apparent diurnal cycle with a maximum value around noon ($\sim$−550 W m^{-2}) and a minimum value during the night ($\sim$−100 W m^{-2}). During the night, the magnitude of NHF loss from the ocean increases from −150 to −250 W m^{-2} in association with ACP events due to an increase in LHF and SHF loss from the ocean (Figure S4e; blue line; Figure S9). With the combined influence of decreasing NSW due to extensive cloud cover and an increase in the LHF and SHF loss from the ocean, the magnitude of ΔNHF is higher for those events that occur during the daytime than during the nighttime (Figures 3c and 4c). Note that the reduction in the large magnitude of ΔNHF in response to the daytime ACP events (Figures 3c and 4c) leads to a sign change in NHF (Figure S4e; black line). For instance, in response to an ACP event that occurs between 1200 and 1800 LST, a NHF gain by the ocean of 400 W m^{-2} becomes a heat loss of −150 W m^{-2} (Figure S4e; black line; Figure S9). For comparison, during
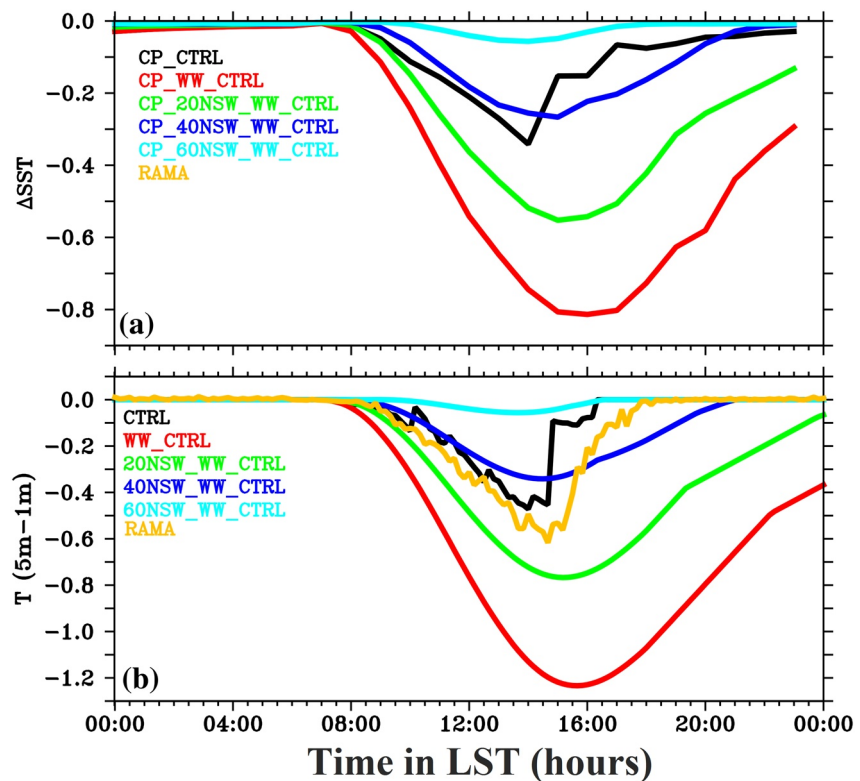
**Figure 12.** The diurnal variability of (a) ΔSST (°C) in the different atmospheric cold pool (ACP) experiments (CP_CTRL-black, CP_WW_CTRL-red, CP_20NSW_WW_CTRL-green, CP_40NSW_WW_CTRL-blue, and CP_60NSW_WW_CTRL-cyan). (b) Difference in temperature between 1 and 5 m (°C) in the control runs (CTRL-black, WW_CTRL-red, 20NSW_WW_CTRL-green, 40NSW_WW_CTRL-blue, and 60NSW_WW_CTRL-cyan) and from the RAMA mooring at 15°N, 90°E (orange; on July 19, 2013). Note that the magnitude of ΔSST varies proportional to the temperature difference between 1 and 5 m (a proxy for the strength of the daytime thermocline.).

the night, there is a climatological average of ~-150 W m^{-2} NHF loss from the ocean during summer and fall in the BoB (Figure S4e; blue line; Figure S9). Thus, daytime ACP events in the BoB during summer and fall can decrease NHF values to their climatological nighttime mean.

Consistent with observations, the maximum value of NHF loss in the ACP experiments during 1700–0700 LST (night) and 0800–1600 LST (daytime) is prescribed as −250 and −150 W m^{-2}, respectively (Figure S5e). Even though high values of NHF loss prescribed during the night is larger than during the day, the magnitude of ΔSST due to ACP events is smaller during the night than the day in the model (Figure 12a), consistent with observations (Figures 3b and 4b). Note that the maximum value of NHF loss prescribed for ACP experiments during 0800–1600 LST (daytime) is constant (−150 W m^{-2}), though ΔSST shows a progressively increasing then decreasing trend during the morning in both the CP_CTRL and CP_WW_CTRL experiments (Figure 12a). These characteristics suggest that diurnal variability of the magnitude of ΔSST with an afternoon peak is not associated with the diurnal variability of ΔNHF.

Two additional experiments were performed to support this argument from a quantitative perspective. In these, NHF loss in the ACP forcing field was increased from −150 to −350 W m^{-2} (defined as CP_WW_CTRL_2NHF; the orange line in Figure 13b) and −150 to −450 W m^{-2} (defined as CP_WW_CTRL_3N-HF; the cyan line in Figure 13b) instead of −150 to −250 W m^{-2} in the CP_WW_CTRL (the pink line in Figure 13b) during the nighttime (0200 LST). In response to the enhancement of NHF loss, the magnitude of ΔSST does not show any significant enhancement in CP_WW_CTRL_2NHF (0.02°C) and CP_ WW_CTRL_3NHF (0.03°C) experiment compared to CP_WW_CTRL (0.02°C) experiment (Figure 13a). Moreover, these values are much smaller than the magnitude of ΔSST in the CP_WW_CTRL experiment during the afternoon (0.8°C). Thus, the observations and model sensitivity experiments suggest that diur-
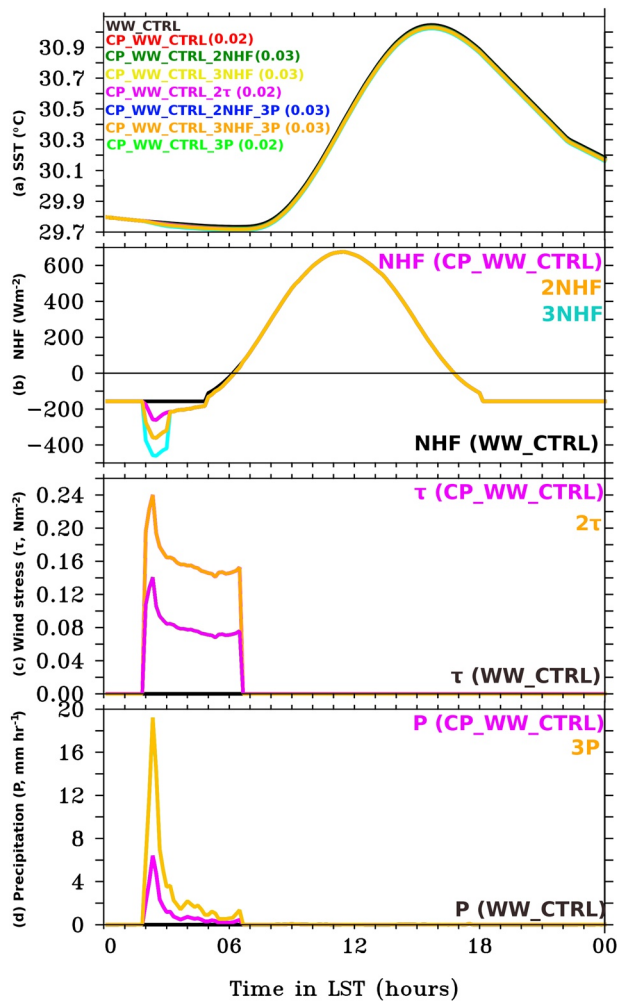
Figure 13. Forcing field used for different atmospheric cold pool (ACP) simulations instead of CP_WW_CTRL during nighttime at 0200 LST: (b) NHF (W m^{-2}): WW_CTRL (black), CP_WW_CTRL (pink; NHF; -150 to -250 W m^{-2}), twofold enhancement of NHF loss with respect to CP_WW_CTRL (orange; 2NHF; -150 to -350 W m^{-2} instead of -150 to -250 W m^{-2} in the CP_WW_CTRL) and threefold enhancement of NHF loss with respect to CP_WW_CTRL (cyan; 3NHF; -150 to -450 W m^{-2} instead of -150 to -250 W m^{-2}). (c) Wind stress (τ; N m^{-2}): WW_CTRL (black), CP_WW_CTRL (pink; τ; $0-0.14$ N m^{-2}), twofold enhancement of τ with respect to CP_WW_CTRL (orange; 2τ; $0-0.24$ N m^{-2} instead of $0-0.14$ N m^{-2}(pink)). (d) Precipitation (P; mm h^{-1}): WW_CTRL (black), CP_WW_CTRL (pink; P; $0-6$ mm h^{-1}), threefold enhancements of P with respect to CP_WW_CTRL (orange; $3P$; $0-18$ mm h^{-1}; instead of $0-6$ mm h^{-1}). (a) Diurnal variability of SST (°C) simulated in the different ACP simulations through the combination of enhancement of NHF (2NHF and 3NHF), wind stress (2τ), and precipitation ($3P$) with respect to CP_WW_CTRL: WW_CTRL (black), CP_WW_CTRL (red), CP_WW_CTRL_2NHF (dark green), CP_WW_CTRL_3NHF (yellow), CP_WW_CTRL_2τ (pink), CP_WW_CTRL_2NHF_3P (blue), CP_WW_CTRL_3NHF_3P (orange), and CP_WW_CTRL_3P (light green). The numbers in the bracket, along with the legends, represent the magnitude of ΔSST (°C) after prescribing the ACP forcing fields during nighttime at 0200 LST in each experiment.

nal variability in the magnitude of ΔNHF is not responsible for a higher magnitude of ΔSST during the daytime than at night.

3.2.4. Role of Wind Speed Enhancement During the ACP Events

The absence of diurnal variability in wind speed enhancement (ΔWS) due to the ACP events is apparent in Figures 3e and 4e. Consistent with this observation, a similar magnitude of wind forcing field is prescribed in all the independent CP_CTRL and CP_WW_CTRL experiments (Figures S5f and S7f; red line). However, ΔSST shows a progressively increasing then decreasing trend during the morning in both the CP_CTRL and CP_WW_CTRL experiments (Figure 12a); even in the absence of enhanced diurnal variability in wind stress during the ACP experiment, a well-defined diurnal variability in the ΔSST is apparent (Figure 12a). These characteristics suggest that the enhancement of wind speed associated with ACP is not responsible for the higher magnitude of ΔSST during the daytime versus the nighttime.

An additional ACP experiment was performed to support this argument, in which wind stress (τ) forcing increased from 0 to 0.25 N m^{-2} (defined as CP_WW_CTRL_2τ) instead of 0–0.14 N m^{-2} in the CP_WW_CTRL during nighttime (0200 LST; Figure 13c). However, in response to the enhanced wind stress, the magnitude of ΔSST does not show any significant enhancement in the CP_WW_CTRL_2τ (0.02°C) experiment compared to CP_WW_CTRL (0.02°C) experiment (Figure 13a). Moreover, the magnitude of ΔSST in CP_WW_CTRL_2τ is much smaller than its magnitude in the CP_WW_CTRL during the afternoon (0.8°C; Figures 12a and 13a). Thus, observations and ACP sensitivity experiments suggest that diurnal variability of ΔWS is not responsible for a higher magnitude of ΔSST during the daytime versus the nighttime.

3.2.5. Role of Precipitation During the ACP

ACPs are always accompanied by intense precipitation. On the one hand, the freshwater flux from the precipitation leads to the formation of a thin freshwater pool in the near-surface layer, which in turn leads to enhanced near-surface stratification due to a reduction in salinity. On the other hand, colder raindrop temperatures can increase the SHF loss from the ocean. Pei et al. (2018) suggest that trapping of NHF loss in a very thin surface freshwater layer formed by the precipitation can also play an important role in determining the SST cooling during ACP events. To examine the net response due to the precipitation, two additional ACP experiments were performed such that precipitation rate increased from 0 to 18 mm h^{-1} (approximately three times) while NHF loss increased from -150 to -350 W m^{-2} (defined as CP_WW_CTRL_2NHF_3P) or -150 to -450 W m^{-2} (defined as CP_WW_CTRL_3NHF_3P) instead of an increase in precipitation 0–6 mm h^{-1} and an increase in NHF loss from -150 to -250 W m^{-2} in the CP_WW_CTRL experiment during nighttime (0200 LST; Figures 13b and 13d). However, the magnitude of ΔSST in CP_WW_CTRL_2NHF_3P (0.03°C) and CP_WW_CTRL_3NHF_3P (0.03°C) do not show any significant difference compared to the CP_WW_CTRL experiment at 0200 LST (Figure 13a). Moreover, the magnitude of ΔSST in CP_WW_CTRL_2NHF_3P is much smaller than its magnitude in the CP_WW_CTRL during the afternoon (0.8°C; Figures 12a and 13a). These details suggest that the trapping of NHF in the shallow near-surface rain-induced freshwater layer is not the reason for higher values of ΔSST in response to ACP events in the afternoon. This

result is distinct from Pei et al. (2018), and is likely associated with the difference in the duration of the ACP event used between these two studies. Pei et al. (2018) studied an ACP event that persists for more than 10 h. However, in the present study, analysis is based on the ACP category single event, which has a typical life span of around 4 h (Figure 2).

3.2.6. Role of the Shallow Daytime Thermocline

The time-depth evolution of temperature before and after an ACP event indicates that the reduction in temperature in response to ACP typically reaches around 5 m depth (Figures 10g–10i and 11g–11i), consistent with observations (Figures 2, 3b and 4b). In addition, cooling in the near-surface layer and subsurface warming in the CP_CTRL and CP_WW_CTRL run compared to their respective control run (CTRL and WW_CTRL) is the typical signature of cooling and deepening of the near-surface layer due to entrainment (Figures 10h, 10i, 11h and 11i). However, an entrainment signature is not apparent in the ACP run during the night in CP_CTRL and CP_WW_CTRL (Figures 10g and 11g).

The presence of a shallow near-surface daytime temperature stratification just below the daytime ML in the upper 5–10 m of the water column in response to solar heating is a common feature in the tropics (Anderson & Riser, 2014; Bernie et al., 2005; Bond & McPhaden, 1995; Mujumdar et al., 2011; Shenoi et al., 2009; Shinoda, 2005). NHF loss during the night leads to the erosion of the shallow vertical temperature gradient associated with the daytime thermocline. The composite of diurnal evolution of temperature difference between 1 and 5 m at the 15°N RAMA mooring in the BoB exhibits a near-zero value during the night and the presence of shallow temperature gradient during the daytime with a higher gradient in fall (0.19°C) than in summer (0.12°C; Figures 3d and 4d; red line). As evident in the observations, the difference in temperature between 1 and 5 m in the CTRL run also shows a clear diurnal cycle, such as its values progressively increase from 0800 to 1000 LST and reach maximum value (0.4°C) around 1400–1600 LST and decrease afterward (Figure 12b; black line; Figures 3d and 4d; red line). Note that the magnitude of shallow near-surface temperature gradient in the CTRL run is comparable with RAMA during a similar period (Figure 12b; black and orange lines).

The presence of a shallow vertical temperature gradient associated with the daytime thermocline leads to thin MLs with reduced heat capacity. Thus, the effects of NHF out of the ocean and the entrainment of cold sub-surface water into the ML through the enhancement of wind speed associated with ACPs will amplify the SST response. Moreover, the strong temporal correspondence between the diurnal variation of the near-surface temperature gradient and ΔSST in response to the ACP forcing in the observations (Figures 3b and 4b-black line and 3d and 4d red line) and model experiments (Figure 12a-black line and Figure 12b-black and orange lines) emphasize the importance of a pre-existing daytime thermocline to determine the difference in magnitude of ΔSST due to ACP events during the day versus the night. In addition, due to the stronger shallow daytime temperature stratification during fall than summer, the magnitude of ΔSST is also higher in the fall than in the summer (Figures 3b, 3d, 4b and 4d).

Note that a temperature gradient still exists below the nighttime ML. However, the magnitude of ΔSST is much smaller during the night compared to the daytime. Consider a 5 m deep daytime ML versus a 15 m deep nighttime ML, both with a constant density of 1,020 kg m^{-3}. A calculation based on Equation 1 indicates that the potential energy of the nighttime ML is nine times higher than the daytime ML; hence, much more kinetic energy is required to erode the ML in the former case than the latter.

Even if the mixing erodes the nighttime ML during an ACP event, the cooling due to entrainment and NHF loss is distributed over a much deeper depth in the case of nighttime ML than a shallow daytime ML. Consider a temperature gradient at the base of ML water column 0.1°C m^{-1} and a deepening of the ML ($\partial h/\partial t$) 5 m h^{-1} due to an ACP event; based on Equation 2, the ACP event will lead to approximately three times more entrainment cooling of SST in the daytime (−0.1°C h^{-1}) than in the nighttime (−0.03°C h^{-1}).

The difference in the diurnal variability of ΔSST and near-surface temperature gradient (1–5 m) between the ACP experiments based on WW_CTRL, 20NSW_WW_CTRL, 40NSW_WW_CTRL, and 60NSW_WW_CTRL are examined to corroborate the connection between the strength of the daytime thermocline and the SST cooling during the ACP events (Figure 12). The purpose of these control runs based on the different intensities of NSW is to create different realizations of the shallow daytime thermocline, such as its strength and persistence is minimum in 60NSW_WW_CTRL and maximum in WW_CTRL experiment
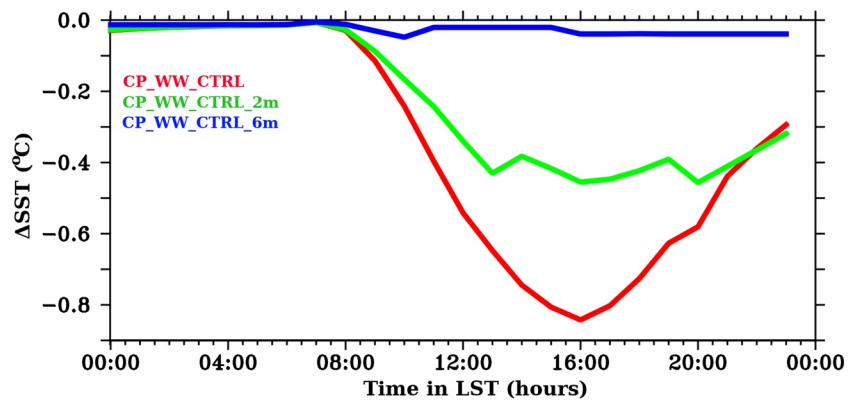
Figure 14. The diurnal variability of ΔSST (°C) in the atmospheric cold pool experiments with different model vertical resolution (1 m—CP_WW_CTRL_1 m-red, 2 m—CP_WW_CTRL_2 m-green, and 6 m—CP_WW_CTRL_6 m-blue).

(Figure 12b). When ACP forcing fields were prescribed in all these experiments, the magnitude of wind stress and NHF are similar. However, the diurnal range of ΔSST is maximum in the CP_WW_CTRL and minimum in CP_60NSW_WW_CTRL (Figure 12a). Note that the only difference in the pre-existing hydrographic conditions between these ACP experiments is in the strength of shallow daytime thermocline. In addition, the magnitude of ΔSST between the ACP experiments varies proportionately with respect to the strength of daytime thermocline (c.f. Figures 12a and 12b).

Note that the strength of daytime shallow temperature gradient associated with daytime thermocline is stronger during fall than summer due to relatively low mean wind speed ($\sim$3 m s^{-1}) during fall versus summer ($\sim$7 m s^{-1}; Figures 1c and 1d and 3–4; red line). Due to the occurrence of the higher magnitude of shallow temperature gradient associated with daytime thermocline during fall, the magnitude of ΔSST due to the ACP during the daytime is higher in the fall than in the summer. This analysis demonstrates that the pre-existing shallow temperature gradient associated with the daytime thermocline, and the associated thin ML, is the primary factor determining the difference in the magnitude of the ACP ΔSST between day and night.

These results suggest that vertical mixing associated with wind speed enhancement and NHF out of the ocean are necessary but not sufficient to generate the SST cooling due to ACP events. Instead, these processes initiate the vertical mixing, and the magnitude of SST drop during ACP events is primarily determined by the trapping of the temperature changes in thin MLs due to shallow near-surface temperature stratification, which is at maximum strength during the daytime.

3.2.7. Impact of Model Vertical Resolution

Our analysis suggests that it is essential to accurately represent the strength of shallow daytime thermocline in the ocean model to simulate the magnitude of SST drop due to the ACP events. We performed additional model runs to examine the sensitivity of our results to the choice of vertical resolution. For that purpose, we carried out two additional control runs similar to WW_CTRL, but with a model vertical resolution of 2 m (WW_CTRL_2 m) and 6 m (WW_CTRL_6 m). We found that the magnitude of ΔSST during the daytime was reduced by a factor of two in CP_WW_CTRL_2 m, and its magnitude was roughly close to its night-time value in CP_WW_CTRL_6 m (Figure 14). These results suggest that ocean models with the high vertical resolution ($\sim$1 m) in the upper 5 m of the water column are essential to resolve ACP-induced SST variability.

4. Summary and Conclusion

Past study has shown that ACP events are plentiful during the summer (May–September) and fall (October–November) in the BoB. However, the modulation of SST in response to intense air-sea interactions associated with ACPs generated from convective systems is not yet documented in the BoB. In this study, we examined whether the time of day of ACP occurrence has any role in determining the magnitude of SST drop. For that purpose, we used moored buoy data with a 10-min temporal resolution at 8°, 12°, and 15°N
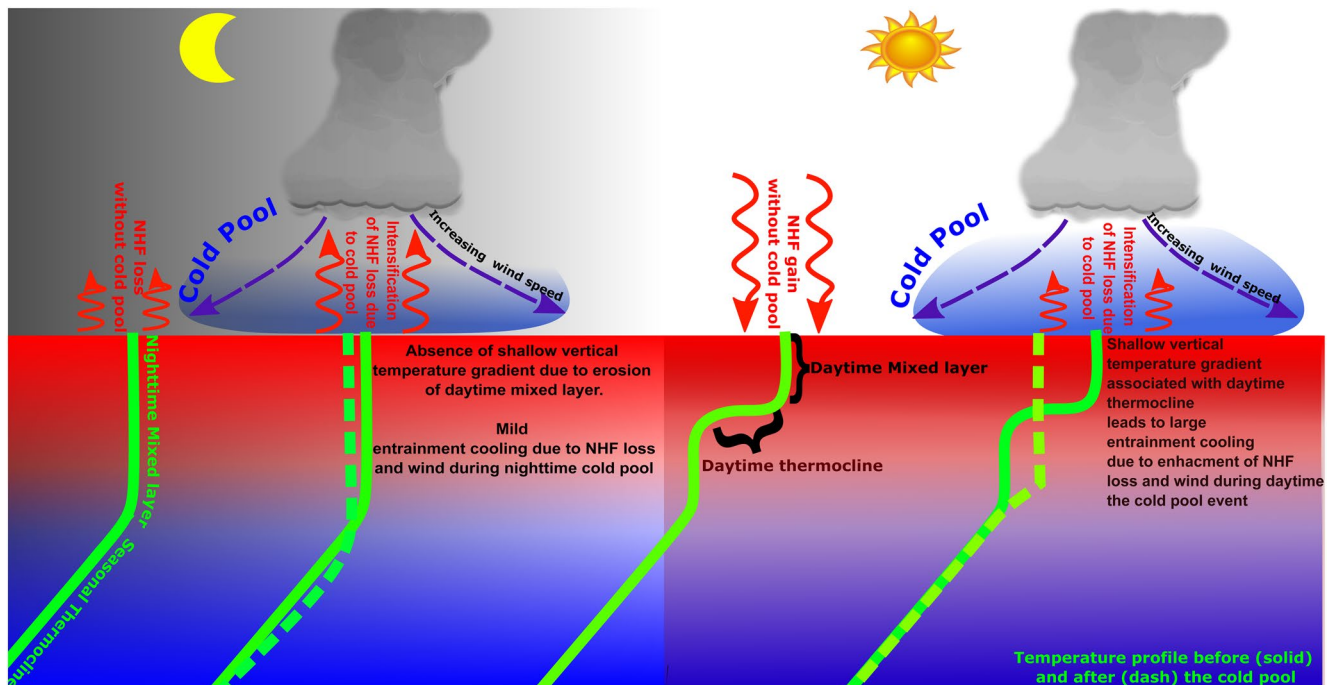
Figure 15. Schematic diagram (not to scale) to illustrate the different mixed layer responses to atmospheric cold pool events during the nighttime and daytime. The red arrow length represents the difference in the magnitude of net surface heat flux (upward indicates heat loss from the ocean).

along with 90°E and PWP one-dimensional ML model focusing on summer and fall when ACPs are most common.

The analysis based on RAMA mooring shows that diurnal variability of reduction in SST (ΔSST) due to ACP events reaches a maximum around 1300–1600 LST (−0.14°C in fall and ∼−0.07°C in summer) and a minimum at night (−0.02°C). In general, the magnitude of ΔSST during the afternoon due to ACPs is a factor of two higher during fall (−0.14°C) than in summer (∼−0.07°C). It is also found that the cooling associated with ACP events is restricted to the upper 10 m of the water column. Approximately 40% (33%) of events at 15° and 12°N (8°N) during summer and ∼32% of events during fall occur between 1000 and 1800 LST when the ACP has more potential to modulate SST.

The analysis based on observation and PWP model experiments suggests that a pre-existing shallow vertical temperature gradient associated with the formation of the daytime thermocline and concomitant shallow MLs is the primary factor determining the enhanced reduction in SST during the afternoon compared to the night. The presence of a shallow vertical temperature gradient associated with the daytime thermocline leads to thin MLs with reduced heat capacity. Thus, the effects of NHF out of the ocean and the entrainment of cold sub-surface water into the ML through the enhancement of wind speed associated with ACPs will amplify the SST response. Our analysis indicates that the absence of a shallow thermocline during the night also requires much more surface forcing to entrain cold seasonal thermocline water to the surface to generate similar cooling as observed during the afternoon due to ACPs. A schematic diagram illustrates the formation of the daytime thermocline and how the presence of shallow near-surface temperature gradient associated with this daytime thermocline determines the higher magnitude of ΔSST during daytime versus nighttime ACP (Figure 15).

The present study suggests that ACP events that occurs during the daytime tends to generate relatively large SST responses with an afternoon peak compared to those occurring at night. Jofia et al. (2021) demonstrate that when ACPs show more frequent and intense activity in the afternoon during the summer, rainfall anomalies cover approximately half of the BoB. The more frequent and intense synoptic-scale ACP activity in the afternoon during summer in the BoB coincides with the period when ACPs have more potential to

generate an SST response. These results highlight the enhancement of ACP events in the afternoon and their impact on SST in the BoB during summer as an important air-sea interaction process.

It is worth pointing out that the magnitude of ΔSST associated with ACP events during the night ($\sim$-0.02 °C) may not be statistically significant. However, the magnitude of ΔSST during summer ($\sim$−0.07 °C) and fall ($\sim$−0.14 °C) associated with ACP events during the afternoon is significant and about 35% of the climatological mean of the diurnal SST range in the study region. These higher magnitude SST perturbations observed during the daytime may not in general have major feedback on the atmosphere, but it is still possible at times for small anomalies on a high mean background SST in the BoB (Figures 1a and 1b) to significantly affect the overlying atmosphere (Palmer & Mansfield, 1984; Samanta et al., 2018; Shankar et al., 2007; Thomson & Vallis, 2018). Also, there may be cumulated effects of frequent cold pool events that arise from nonlinearities in air-sea interactions. Hence, a quantitative understanding of how ACP events affect SST is valuable for assessing coupled model performance in regions where ACP events frequently occur. In addition, recent studies have shown that the increasing SST trend associated with global warming can enhance near-surface thermal stratification (e.g., Roxy et al., 2016). The present study demonstrates that a pre-existence shallow temperature gradient and thin ML is an essential pre-condition to generating an SST response due to ACP events; hence, it is possible that the enhancement of near-surface thermal stratification due to global warming may increase the SST response due to ACP events in the future.

Past studies have suggested that it is crucial to simulate the diurnal cycle of SST to accurately represent the magnitude of intraseasonal and seasonal SST variability in the ocean models (Bernie et al., 2005; Mujumdar et al., 2011; Shinoda, 2005; Thushara & Vinayachandran, 2014). The present study also suggests that it is essential to accurately represent the strength of shallow daytime thermocline and the depth of the ML in ocean models to simulate the magnitude of SST drops due to the ACP events. The typical vertical resolution of ocean general circulation models is around 5–10 m in the upper water column (Ravichandran et al., 2013). Hence, the present study indictes the need for models with the high vertical resolution ($\sim$1 m) in the upper 5 m of the water column to resolve ACP induced SST variability. In addition, past studies have highlighted that it is imperative to accurately represent the intraday variation of SST in coupled models to simulate the diurnal scale coupling between the ocean and atmosphere, which in turn has a significant role in determining the seasonal and intraseasonal variability (Johnson & Ciesielski, 2017; Johnson et al., 1999; Ruppert & Johnson, 2016; Seo et al., 2014; Slingo et al., 2003; Webster et al., 1996). The present study highlights the importance of accurately representing ACP activity in the BoB and associated air-sea interaction processes that affect the diurnal SST cycle in coupled models, which will lead not only to better simulations but also to potentially more skillful seasonal and extended range weather predictions.

Data Availability Statement

RAMA data quality controlled and distributed by Global Tropical Moored Buoy Array (GTMBA) project office of NOAA/Pacific Marine Environmental Laboratory, RAMA data are available from PMEL (https://www.pmel.noaa.gov/gtmba/pmel-theme/indian-ocean-rama). Microwave OI SST data are produced by Remote Sensing Systems and sponsored by National Oceanographic Partnership Program (NOPP) and the NASA Earth Science Physical Oceanography Program. Data are available at www.remss.com. MODIS Aqua chlorophyll data is distributed by NOAA Coast Watch, and data is available at https://oceanwatch.pfeg.noaa.gov/thredds/Satellite/MH1/chla/catalog.html?dataset=satellite/MH1/chla/8day. CCMP Version-2.0 vector wind analyses are produced by Remote Sensing Systems. Data are available at www.remss.com.The Matlab code of PWP model used in this study is obtained from https://github.com/OceanMixingGroup/mixingsoftware/tree/master/pwp. This is INCOIS contribution number 434 and PMEL contribution number 5209.

References

Anderson, J. E., & Riser, S. C. (2014). Near-surface variability of temperature and salinity in the near-tropical ocean: Observations from profiling floats. *Journal of Geophysical Research: Oceans*, *119*, 7433–7448. https://doi.org/10.1002/2014JC010112

Atlas, R., Hoffman, R. N., Ardizzone, J., Leidner, S. M., Jusem, J. C., Smith, D. K., & Gombos, D. (2011). A cross-calibrated, multiplatform ocean surface wind velocity product for meteorological and oceanographic applications. *Bulletin of the American Meteorological Society*, *92*, 157–174. https://doi.org/10.1175/2010BAMS2946.1

Babu, K. N., Sharma, R., Agarwal, N., Agarwal, V. K., & Weller, R. A. (2004). Study of the mixed layer depth variations within the north Indian Ocean using a 1-D model. *Journal of Geophysical Research*, *109*, C08016. https://doi.org/10.1029/2003JC002024

Bernie, D. J., Woolnough, S. J., Slingo, J. M., & Guilyardi, E. (2005). Modeling diurnal and intraseasonal variability of the ocean mixed layer. *Journal of Climate*, *18*, 1190–1202. https://doi.org/10.1175/JCLI3319.1

Bond, N. A., & McPhaden, M. J. (1995). An indirect estimate of the diurnal cycle in upper ocean turbulent heat fluxes at the equator, 140°W. *Journal of Geophysical Research*, *100*, 18369–18378. https://doi.org/10.1029/95jc01592

Buckley, J. M., Mingels, B., & Tandon, A. (2019). The impact of lateral advection on SST and SSS in the northern Bay of Bengal during 2015. *Deep-Sea Research Part II: Topical Studies in Oceanography*, *172*, 104653. https://doi.org/10.1016/j.dsr2.2019.104653

Chaudhuri, D., Sengupta, D., D'Asaro, E., Venkatesan, R., & Ravichandran, M. (2019). Response of the salinity-stratified Bay of Bengal to Cyclone Phailin. *Journal of Physical Oceanography*, *49*, 1121–1140. https://doi.org/10.1175/jpo-d-18-0051.1

Clayson, C. A., & Weitlich, D. (2007). Variability of tropical diurnal sea surface temperature. *Journal of Climate*, *20*, 334–352. https://doi.org/10.1175/JCLI3999.1

Cronin, M. F., & McPhaden, M. J. (1999). Diurnal cycle of rainfall and surface salinity in the Western Pacific Warm Pool. *Geophysical Research Letters*, *26*(23), 3465–3468. https://doi.org/10.1029/1999GL010504

de Szoeke, S. P., Skyllingstad, E. D., Zuidema, P., & Chandra, A. S. (2017). Cold pools and their influence on the tropical marine boundary layer. *Journal of the Atmospheric Sciences*, *74*, 1149–1168. https://doi.org/10.1175/JAS-D-16-0264.1

Edson, J. B., Jampana, V., Weller, R. A., Bigorre, S. P., Plueddemann, A. J., Fairall, C. W., et al. (2013). On the exchange of momentum over the open ocean. *Journal of Physical Oceanography*, *43*, 1589–1610. https://doi.org/10.1175/JPO-D-12-0173.1

Fairall, C. W., Bradley, E. F., Hare, J. E., Grachev, A. A., & Edson, J. B. (2003). Bulk parameterization of air-sea fluxes: Updates and verification for the COARE Algorithm. *Journal of Climate*, *16*, 571–591. https://doi.org/10.1175/1520-0442(2003)016<0571:BPOASF>2.0.CO;2

Gentemann, C. L., Wick, G. A., Cummings, J. & Bayler, E. (2004). *Multi-sensor improved sea surface temperature (MISST) for GODAE*. Paper presented at 13th Conference on Satellite Meteorology and Oceanography. Retrieved from http://www.remss.com/papers/gentemann/gentemann_13satmet_2004.pdf

Girishkumar, M. S., Joseph, J., Thangaprakash, V. P., Pottapinjara, V., & McPhaden, M. J. (2017). Mixed layer temperature budget for the northward propagating Summer Monsoon Intraseasonal Oscillation (MISO) in the central Bay of Bengal. *Journal of Geophysical Research*, *122*, 8841–8854. https://doi.org/10.1002/2017JC013073

Jerlov, N. G. (1968). *Optical oceanography, oceanography series* (Vol. 5). Elsevier.

Jiang, X., & Li, J. (2011). Influence of the annual cycle of sea surface temperature on the monsoon onset. *Journal of Geophysical Research*, *116*, D10105. https://doi.org/10.1029/2010JD015236

Jofia, J., Girishkumar, M. S., McPhaden, M. J., & Pattabhi Ram Rao, E. (2021). Diurnal variability of atmospheric cold pool events and associated air-sea interactions in the Bay of Bengal during the summer monsoon. *Climate Dynamics*, *56*, 837–853. https://doi.org/10.1007/s00382-020-05506-w

Johnson, R. H., & Ciesielski, P. E. (2017). Multiscale variability of the atmospheric boundary layer during DYNAMO. *Journal of the Atmospheric Sciences*, *74*, 4003–4021. https://doi.org/10.1175/jas-d-17-0182.1

Johnson, R. H., Rickenbach, T. M., Rutledge, S. A., Ciesielski, P. E., & Schubert, W. H. (1999). Trimodal characteristics of tropical convection. *Journal of Climate*, *12*, 2397–2418. https://doi.org/10.1175/1520-0442(1999)012<2397:tcotc>2.0.co;2

Kantha, L., Weller, R., Farrar, J. T., Rahaman, H., & Jampana, V. (2019). A note on modeling mixing in the upper layers of the Bay of Bengal: Importance of water type, water column structure, and precipitation. *Deep Sea Research Part II: Topical Studies in Oceanography*, *168*, 104643. https://doi.org/10.1016/j.dsr2.2019.104643

Li, Y., Han, W., Shinoda, T., Wang, C., Lien, R.-C., Moum, J. N., & Wang, J.-W. (2013). Effects of the diurnal cycle in solar radiation on the tropical Indian Ocean mixed layer variability during wintertime Madden-Julian oscillations. *Journal of Geophysical Research: Oceans*, *118*, 4945–4964. https://doi.org/10.1002/jgrc.20395

Lotliker, A. A., Omand, M. M., Lucas, A. J., Laney, S. R., Mahadevan, A., & Ravichandran, M. (2016). Penetrative radiative flux in the Bay of Bengal. *Oceanography*, *29*(2), 214–221. https://doi.org/10.5670/oceanog.2016.53

McPhaden, M. J., Meyers, G., Ando, K., Masumoto, Y., Murty, V. S. N., Ravichandran, M., et al. (2009). RAMA: The research moored array for African-Asian-Australian monsoon analysis and prediction a new moored buoy array in the historically data-sparse Indian Ocean provides measurements to advance monsoon research and forecasting. *Bulletin of the American Meteorological Society*, *90*, 459–480. https://doi.org/10.1175/2008BAMS2608.1

Morel, A. (1988). Optical modeling of the upper ocean in relation to its biogenous matter content (case I waters). *Journal of Geophysical Research*, *93*, 1652–1665. https://doi.org/10.1029/jc093ic09p10749

Mujumdar, M., Salunke, K., Rao, S. A., Ravichandran, M., & Goswami, B. (2011). Diurnal cycle induced amplification of sea surface temperature intraseasonal oscillations over the Bay of Bengal in summer monsoon season. *IEEE Geoscience and Remote Sensing Letters*, *99*, 206–210. https://doi.org/10.1109/lgrs.2010.2060183

Navaneeth, K. N., Martin, M. N., Jossia Joseph, K., & Venkatesan, R. (2019). Contrasting the upper ocean response to two intense cyclones in the Bay of Bengal. *Deep-Sea Research Part I: Oceanographic Research Papers*, *147*, 65–78. https://doi.org/10.1016/j.dsr.2019.03.010

Palmer, T. N., & Mansfield, D. A. (1984). Response of two atmospheric general circulation models to sea-surface temperature anomalies in the tropical east and west Pacific. *Nature*, *310*, 483–485. https://doi.org/10.1038/310483a0

Paulson, C. A., & Simpson, J. J. (1977). Irradiance measurements in the upper ocean. *Journal of Physical Oceanography*, *77*, 952–956. https://doi.org/10.1175/1520-0485(1977)007<0952:IMITUO>2.9.CO

Pei, S., Shinoda, T., Soloviev, A., & Lien, R. -C. (2018). Upper ocean response to the atmospheric cold pools associated with the Madden-Julian Oscillation. *Geophysical Research Letters*, *45*, 5020–5029. https://doi.org/10.1029/2018gl077825

Price, J. F., Weller, R. A., & Pinkel, R. (1986). Diurnal cycling: Observations and models of the upper ocean response to diurnal heating, cooling and wind mixing. *Journal of Geophysical Research*, *91*(C7), 8411–8427. https://doi.org/10.1029/JC091iC07p08411

Ravichandran, M., Behringer, D., Sivareddy, S., Girishkumar, M. S., Chacko, N., & Harikumar, R. (2013). Evaluation of the global ocean data assimilation system at INCOIS: The tropical Indian Ocean. *Ocean Modelling*, *69*, 123–135. https://doi.org/10.1016/j.ocemod.2013.05.003

Roxy, M., & Tanimoto, Y. (2007). Role of SST over the Indian Ocean in influencing the intraseasonal variability of the Indian summer monsoon. *Journal of the Meteorological Society of Japan*, *85*, 349–358. https://doi.org/10.2151/jmsj.85.349

Roxy, M. K., Modi, A., Murtugudde, R., Valsala, V., Panickal, S., Prasanna Kumar, S., et al. (2016). A reduction in marine primary productivity driven by rapid warming over the tropical Indian Ocean. *Geophysical Research Letters*, *43*(2), 826–833. https://doi.org/10.1002/2015GL066979

Ruppert, J. H., Jr, & Johnson, R. H. (2016). On the cumulus diurnal cycle over the tropical warm pool. *Journal of Advances in Modeling Earth Systems*, *8*, 669–690. https://doi.org/10.1002/2015MS000610

Samanta, D., Hameed, S. N., Jin, D., Thilakan, V., Ganai, M., Rao, S. A., & Deshpande, M. (2018). Impact of a narrow coastal Bay of Bengal sea surface temperature front on an Indian summer monsoon simulation. *Scientific Reports*, *8*, 17694. https://doi.org/10.1038/s41598-018-35735-3

Seo, H., Subramanian, A. C., Miller, A. J., & Cavanaugh, N. R. (2014). Coupled impacts of the diurnal cycle of sea surface temperature on the Madden-Julian Oscillation. *Journal of Climate*, *27*, 8422–8443. https://doi.org/10.1175/JCLI-D-14-00141.1

Shankar, D., Shetye, S., & Joseph, P. V. (2007). Link between convection and meridional gradient of sea surface temperature in the Bay of Bengal. *Journal of Earth System Science*, *116*, 385–406. https://doi.org/10.1007/s12040-007-0038-y

Shenoi, S. S. C., Nasnodkar, N., Rajesh, G., Joseph, K. J., Suresh, I., & Almeida, A. M. (2009). On the diurnal ranges of sea surface temperature (SST) in the north Indian Ocean. *Journal of Earth System Science*, *118*(5), 483–496. https://doi.org/10.1007/s12040-009-0038-1

Shenoi, S. S. C., Shankar, D., & Shetye, S. (2002). Differences in heat budgets of the near-surface Arabian Sea and Bay of Bengal: Implications for the summer monsoon. *Journal of Geophysical Research*, *107*(C6). https://doi.org/10.1029/2000JC000679

Shinoda, T. (2005). Impact of the diurnal cycle of solar radiation on intraseasonal SST variability in the Western Equatorial Pacific. *Journal of Climate*, *18*, 2628–2636. https://doi.org/10.1175/jcli3432.1

Slingo, J. M., Inness, P., Neale, R., Woolnough, S., & Yang, G.-Y. (2003). Scale interactions on diurnal to seasonal timescales and their relevance to model systematic errors. *Annals of Geophysics*, *46*, 139–155

Sutherland, G., Marié, L., Reverdin, G., Christensen, K. H., Broström, G., & Ward, B. (2016). Enhanced turbulence associated with the diurnal jet in the ocean surface boundary layer. *Journal of Physical Oceanography*, *46*, 3051–3067. https://doi.org/10.1175/jpo-d-15-0172.1

Thomson, S. I., & Vallis, G. K. (2018). Atmospheric response to SST anomalies. Part II: Background-state dependence, teleconnections, and local effects in summer. *Journal of the Atmospheric Sciences*, *75*, 4125–4138. https://doi.org/10.1175/JAS-D-17-0298.1

Thushara, V., & Vinayachandran, P. N. (2014). Impact of diurnal forcing on intraseasonal sea surface temperature oscillations in the Bay of Bengal. *Journal of Geophysical Research: Oceans*, *119*, 8221–8241. https://doi.org/10.1002/2013JC009746

Webster, P. J., Clayson, C. A., & Curry, J. A. (1996). Clouds, radiation, and the diurnal cycle of sea surface temperature in the tropical western Pacific. *Journal of Climate*, *9*, 1712–1730. https://doi.org/10.1175/1520-0442(1996)009<1712:cratdc>2.0.co;2

Weller, R. A., Farrar, J. T., Buckley, J., Mathew, S., Venkatesan, R., SreeLekha, J., et al. (2016). Air-sea interaction in the Bay of Bengal. *Oceanography*, *29*(2), 28–37. https://doi.org/10.5670/oceanog.2016.36

Wenegrat, J. O., & McPhaden, M. J. (2015). Dynamics of the surface layer diurnal cycle in the equatorial Atlantic Ocean (0°, 23°W). *Journal of Geophysical Research: Oceans*, *120*, 563–581. https://doi.org/10.1002/2014JC010504

Wielicki, B. A., Barkstrom, B. R., Harrison, E. F., Lee, R. B., Smith, G. L., & Cooper, J. E. (1996). Clouds and the Earth's Radiant Energy System (CERES): An earth observing system experiment. *Bulletin of the American Meteorological Society*, *77*, 853–868. https://doi.org/10.1175/1520-0477(1996)077<0853:CATERE>2.0.CO;2

Yokoi, S., Katsumata, M., & Yoneyama, K. (2014). Variability in surface meteorology and air-sea fluxes due to cumulus convective systems observed during CINDY/DYNAMO. *Journal of Geophysical Research - D: Atmospheres*, *119*, 2064–2078. https://doi.org/10.1002/2013JD020621